Atomistic Investigation of Morphology and Optoelectronic Properties of Bismuth Sulfide Nanostructures

Philosofiæ Doctor Thesis

Vasco Calzia

Dottorato in Fisica - XXVII Ciclo

Università degli Studi di Cagliari

FIS/03

Tutor

Prof. Giovanni Bongiovanni

Co-Tutor

Dott. Alessandro Mattoni

Coordinatore

Prof. Paolo Ruggerone

PhD School Coordinator: Prof. Paolo Ruggerone

Reviewer: Dott. Nicola Seriani

Day of the defense: XXth May 2015

Signature from head of PhD committee

Abstract

Nanostructured metal sulfides (MS) have attracted great interest in recent years because of the possibility to synthesize nanoparticles from solution and tuning their optoelectronic properties through quantum confinement phenomena. A large number of applications have been reported in the field of solar cells, light-emitting diodes, lithium-ion batteries, thermoelectric devices, sensors, fuel cells and nonvolatile memory devices. Among the large family of semiconductor sulfides, the present Thesis is focussed on bismuthinite. The choice was motivated by a combination of factors. Its non-toxicity, low cost synthesis and high absorption properties make Bi_2S_3 a promising material for several application, such as solid-state semiconductor-sensitized solar cells. The intrisic anisotropy in the crystal structure of this material facilitates the formation of elongated nanostructures, in particular nanorods, nanoribbons, and nanowires. These structures find important applications in many nanodevices, for example field emitters, solar cells, and lithium-ion batteries.

On the other hand, researchers are still far from a complete understanding of Bi_2S_3 properties. The colloidal synthesis of bismuthinite nanostructures, although cheap and environmentally friendly, does not allow a perfect control on stoichiometry and surface passivation. The large majority of the experimental studies does not report photoluminescence of the nanocrystals, which indicates the presence of trap states and a low defect tolerance of the material. These facts cause a lower efficiency of the devices based on Bi_2S_3 nanoparticles with respect to anologous system based on other nanomaterials (e.g Sb_2S_3 in solid-state sensitized solar cells). The absence of linear optical data makes more difficult to investigate the electronic structure of

the material by means of spectroscopic techniques. Ab initio atomistic simulations represent a valid alternative to get an insight on the optoelectronic properties of bismuth sulfide. Despite some computational work on bulk Bi_2S_3 is already present in literature, there are currently no ab initio studies concerning nanostructures of this material. Such lack of information motivates the work of the present thesis that focuses on the investigation of morphology and electronic properties of Bi_2S_3 nanocrystals.

The thesis is organized as follows. In the first chapter the main differences and advantages of nanostructured materials over the bulk counterpart are presented. I put the accent on metal sulfide nanocrystals, in particular those of the Bi_2S_3 family (pnictogen chalcogenide) and their application in several fields of physics, environmental science, and engineering. A section is reserved to report the development of elongated semiconductor nanostructures and their peculiarity with respect to nanocrystals with lower aspect ratio.

The second chapter describes the computational and experimental methods used in this study. The basic concepts of density functional theory and its implementation in quantum-chemistry codes are reported. A description of the synthesis and spectroscopic methods used to check the validity of the theoretical predictions is also given. For the detailed list of the basis sets, pseudopotentials, and exchange-correlation functionals used in each calculation I refer to the end of Chapter 3 and 4.

Chapter 3 deals with the bulk properties of Bi_2S_3. Atomic and crystal cell relaxation are performed. Also I investigated electronic properties from the calculation of the band structure, density of states, and efficient mass. These simulations are an important preliminary to the study of Bi_2S_3 nanostructures. By comparing my results with the previous studies present in literature it is possible to validate the method (functionals, pseudopotentials, etc) and proceed with the study of unexplored systems.

Chapter 4 investigates the properties of Bi_2S_3 nanostructures. First, I focus on elongated nanoribbons (that are the building blocks of the crystal structure) and study saturated and unsaturated nanocrystals of finite size in comparison with one-dimensional infinite ones. By means of (time-dependent) density functional theory calculations it is demonstrated that the optical gap can be tuned through quantum confinement with sizable effects for nanoribbons smaller than three nanometers. A comparison with Sb_2S_3, shown that Bi_2S_3 nanostructures have similar tunability of the band gap and a better tendency of passivating defects at the (010) surfaces through local reconstruction. Then, the focus shifts over ultrathin nanowires formed by the aggregation of a small number of nanoribbons, with lateral sizes as small as 3 nm as in fact observed by transmission electron microscopy. Their electronic properties are investigated finding that surfaces induce peculiar 1D-like electronic states on the nanowire edges that are located 300 meV above the valence band. Sulfur vacancies are also responsible for localized states a few hundreds meV below the conduction band. The possibility to remove the surface-induced intragap states is further investigated by passivating the surfaces of the nanowires with carboxylic and amine groups that are commonly employed in colloidal synthesis. The small methylamine and acetic acid molecules are expected to fully passivate the surfaces of the nanowires removing the edge states and restoring a clean band gap.

Conclusions are finally reported in Chapter 5. The results of the present Thesis provide a characterization of the energetics and optoelectronic properties of bismuth sulfide nanostructures showing the relevance of surface defects and suggesting a possible route for improving optoelectronic properties of Bi_2S_3 nanostructures by tuning the size of the ligand molecules.

List of publications of the author

- **Atomistic Investigation of the Solid-Liquid Interface between the Crystalline Zinc Oxide Surface and the Liquid Tetrahydrofuran Solvent**
  Maria Ilenia Saba, Vasco Calzia, Claudio Melis, Luciano Colombo, and Alessandro Mattoni
  The Journal of Physical Chemistry C **2012** 116 (23), 12644-12648
  DOI: 10.1021/jp302700b

- **Electronic Properties and Quantum Confinement in Bi2S3 Ribbon-Like Nanostructures**
  V. Calzia, G. Malloci, G. Bongiovanni, and A. Mattoni
  The Journal of Physical Chemistry C **2013** 117 (42), 21923-21929
  DOI: 10.1021/jp405740b

- **Colloidal Bi2S3 Nanocrystals: Quantum Size Effects and Midgap States**
  M. Aresti, M. Saba, R. Piras, D. Marongiu, G. Mula, F. Quochi, A. Mura, C. Cannas, M. Mureddu, A. Ardu, G. Ennas, V. Calzia, A. Mattoni, A. Musinu, and G. Bongiovanni
  Advanced Functional Materials **2014** 24 (22), 3341-3350
  DOI: 10.1002/adfm.201303879

- **Colloidal synthesis and characterization of Bi2S3 nanoparticles for photovoltaic applications**
  R. Piras, M. Aresti, M. Saba, D. Marongiu, G. Mula, F. Quochi, A. Mura, C. Cannas, M. Mureddu, A. Ardu, G. Ennas, V. Calzia, A. Mattoni, A. Musinu and G. Bongiovanni
  J. Phys.: Conf. Ser. **566** 012017
  DOI:10.1088/1742-6596/566/1/012017

- **Synthesis and Atomistic Modeling of Ultrathin Bi2S3 Nanowires: Surfaces, Defects and Passivation**
  V. Calzia, R. Piras, A. Ardu, A. Musinu, G. Bongiovanni, M. Saba, and A. Mattoni (submitted)

- **Pinpointing the Cause of Platinum Tipping on CdS Nanorods**
  C. Caddeo, V. Calzia, L. Bagolini, M. Lusk, and A. Mattoni (submitted)

Acknowledgements

This work has been funded by Sardinia Regional Government PhD scholarship (P.O.R. Sardegna F.S.E. Operational Program of the Autonomous Region of Sardinia, European Social Fund 2007-2013 - Axis IV Human Resources, Objective l.3, Line of Activity l.3.1.), by Sardinia Regional Government under L. R. 7/2007 CRP3_114 "Design di nanomateriali ibridi organici/inorganici per l'energia fotovoltaica" and CRP-249078 "Nanomateriali ecocompatibili per celle fotovoltaiche a stato solido di nuova generazione", by the Italian Institute of Technology under Project Seed "POLYPHEMO" (grant n° B21J0000290007), by (MIUR Under PON 2007-2013 (Project NETERGIT), and by Consiglio Nazionale delle Ricerche (Progetto Premialit RADIUS). I acknowledge computational support by IIT Platform "Computation" and by CINECA through ISCRA Initiative (Projects OPTO-BIS and SURF-BIS). I gratefully acknowledges my advisors Prof. Giovanni Bongiovanni and Dr. Alessandro Mattoni for all the support given.

Contents

List of Figures

LIST OF FIGURES

1

Introduction

In the last decades, nanomaterials attracted the attention of the scientific community due to their peculiar properties with respect to their bulk counterpart. When the extent of a solid is reduced in one or more dimensions, the physical, magnetic, electrical and optical properties can be dramatically altered. This makes nanostructures a subject of both fundamental and practical interest; their properties can be taylored by controlling the size and shape on the nanometer scale. One class of effects is related to their large surface-to-volume ratio. For a

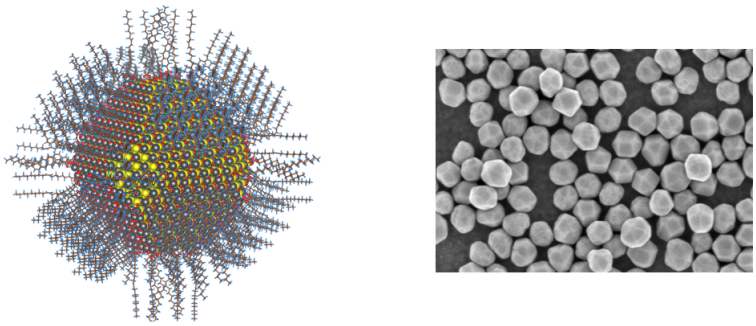

Figure 1.1: Left: Semiconductor nanoparticle (quantum dot) of lead sulfide with complete passivation by oleic acid, oleyl and hydroxyl (size ∼5nm). Right: Scanning electron microscope image of 100 nm stabilized gold nanoparticles(1).

spherical nanoparticle of radius R composed of atoms of average spacing a, the

ratio between the atoms at the surface N_{surf} and the overall atoms N is given by

$$\frac{N_{surf}}{N} \approx \frac{3a}{R} \tag{1.1}$$

For $R = 6a \sim 1$ nm, half of the atoms are on the surface. The large surface area of the nanoparticles is advantageous, for example, in catalysis applications, where reactions occur at the surface of the catalyst, or in gas storage applications, where molecules are adsorbed on the surface. The large surface has also drastic effects on the stability of the nanoparticles. The cohesive energy is lowered because atoms

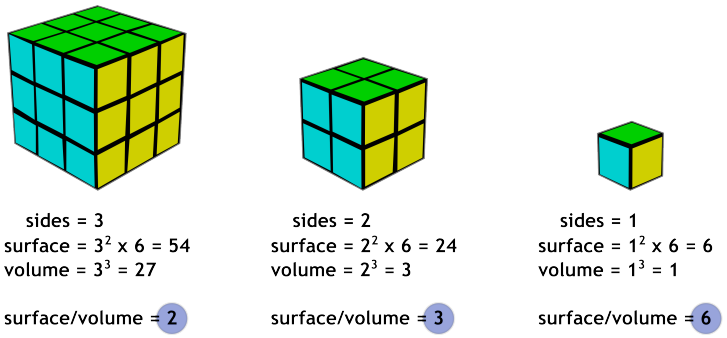

Figure 1.2: A conceptual illustration that describes the increase of the surface-to-volume ratio of the nanomaterials when the nanoparticles become smaller.

on the surface are incompletely bound. As a consequence, nanoparticles melt at temperature far below the melting temperature of the corresponding bulk solid. From an optoelectronic point of view, a characteristic feature of semiconductor nanoparticles is the size dependency of the band gap when the dimension of the nanocrystal is lower than the excitonic radius of the material. This effect is known as *quantum confinement* (QC). The tuning of the band gap through QC finds several applications in optoelectronic devices. For example, it can be useful in solar cells in order to set up the light absorption edge at the desidered wavelength.

The present Thesis is focused on nanostructures of bismuth sulfide (Bi_2S_3), a metal sulfide semiconductor of the pnictogen chalcogenides family. Metal sulfides has acquired a prestigious place in nanoscience and engineering, thanks to their abundance in nature as minerals, their facile synthesis through bottom-up

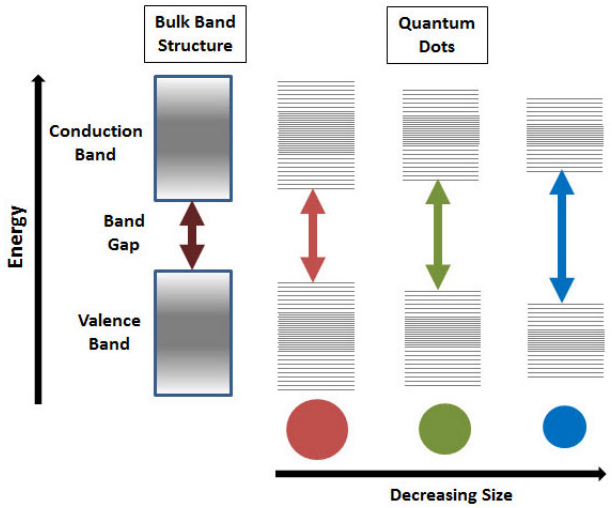

Figure 1.3: The effects of the quantum confinement on the electronic structure of a semiconductor material. The bulk material present a continuum of filled (valence bands) and empty states (conduction bands) with a band gap in between. As the nanocrystals get smaller a smaller, the band gap becomes larger and the energy levels become discretized.

techniques and unique optoelectronic properties for both fundamental physics research and application in devices. However, the toxicity of some of their more important representatives (such as CdS and Sb_2S_3) has led to the research of new metal sulfide compounds that could overcome this problem maintaining, at the same time, the previously cited properties. Another urge of the present research is the possibility to manufacture elongated nanostructures with particularly stringent size and optoelectronic properties. Bi_2S_3 satisfies all these requirements. In fact, it is an environmentally friendly material whose anisotropic crystal structure facilitates the synthesis of elongated nanostructures.

In this chapter, it will be given a short review of the numerous applications of metal sulfides in a large spectrum of fields. Also, the topic of semiconductor elongated nanostructures is presented. It will be shown how the pnictogen chalcogenides (in particular Bi_2S_3) can potentially assume a preminent role for the synthesis of high aspect ratio nanostructures.

1.1 Metal sulfides nanostructures

Nanomaterials are currently a topic of great interest for the scientific community thanks to their electrical, optical, magnetic and mechanical properties which show a combination of surface and bulk features(7, 8, 9). Outstanding results have been achieved in the fields of energy conversion and energy storage devices(10), but a deeper understanding of the nanomaterials properties is still needed.

Nanostructured metal sulfides (MS) have been studied to better understand quantum size effects and for their applications in solar cells, light-emitting diodes, lithium-ion batteries, thermoelectric devices, sensors, fuel cells and nonvolatile memory devices(11, 12, 13).They are abundant and cheap, and belong to a class of minerals characterized by several structural types.

Among the numerous techniques used to synthesize MS nanostructures, we mention solution-phase reactions (11), hydrothermal growth (14), physical vapor deposition (PVD)(15, 16) and chemical vapor deposition (CVD) (17). Biomolecule-assisted (18) and colloidal (19, 20) synthesis represent a possible non-toxic route of MS nanostructures.

One-dimensional nanostructured ZnS and CdS have received great attention for various optoelectronic applications, such as waveguides, field-effect transistors, lasers, solar cells, photodetectors, thin film electroluminescent displays and light emitting diodes(21). Wide-bandgap MS nanostructures are good electrically driven lasing materials and active optical waveguide materials, which may find extensive application in near-field optical lithography and telecommunications(22). II-VI group MS quantum dots are particulary suitable for band gap modulation through quantum confinement, allowing the design of devices with tunable physical properties(23, 24). Limitations come mainly from the presence of defects, the lack of doping reproducibility, and the difficulty to obtain monocrystalline nanostructures.

Metal ion doped metal sulfide nanomaterials are promising photocatalysts for the degradation of organic pollutants in water and environmental protection technologies. In particular CdS, CuS, ZnS, Bi_2S_3 and Sb_2S_3 have been used for the development of visible-light sensitive photocatalysts (25, 26). Doping of metal ions has been used for the wide band gap MS photocatalysts(27).

ZnS and CdS nanostructures are also interesting nanomaterials for photovoltaics and photodetectors(21, 28) due to their excellent photoelectrical properties. In particular the high photosensitivity and fast response of ZnS and other doped semiconducting MS nanostructures have been employed in systems for optical switches, sensors and photodetectors in the visible light region(29).

Bi_2S_3, Sb_2S_3, and PbS nanostructures show potential thermoelectric applications(30, 31). Their thermoelectric power factor is greater in the nanocrystalline form than in the bulk and comparable to that of the most indicated materials used so far. Moreover, they have potential applications in solid-state power generation from heat sources(32).

In the field of energy storage, the high capacity, high lithium activity and low cost of MS make them interesting cathode materials for lithium-ion batteries(33). Transition metal sulfides, such as NiS and CoS, exhibit potential applications in solid oxide fuel cells(34).

Amorphous molybdenum sulfide films is a valid active non-precious catalysts for hydrogen evolution in water, in alternative to the much more expensive Pt and its composites(35, 36). Hydrogen can also be stored in nanostructured materials through electrochemical processes in aqueous solutions under moderate conditions. Thanks to their large surface area, high surface reactivity and strong gas adsorption, MoS_2 nanotubes and Bi_2S_3 nanorods are ideal nanomaterials for hydrogen storage(37, 38).

In the field of energy conversion, Cu_2S nanocrystals in combination with CdS nanorods have found important application in solution-processed solar cells on both flexible plastic substrates and glass substrates, showing a long-term stability(11, 39). Moreover, Cu_2S can be used as an excellent light absorber in ultrathin absorber solar cells thanks to its low cost, non-toxicity, and good absorption properties(40). The ternary I-III-VI chalcogenide chalcopyrites ($CuMX_2$) (M = In, Ga and X = S, Se) exhibit power efficiencies close to 20% (12, 41, 42). Their direct band gap in the red edge of the solar spectrum, and their stability under long-term excitation makes them interesting materials for photovoltaic applications.

MS nanostructures find also application in dye-sensitized solar cells (DSSCs) thanks to their high optical absorption coefficient and low cost(43, 44). FeS, FeS_2

and NiS nanostructures have been used as photocathodes in tandem solar cells with dye-sensitized TiO_2 nanostructures as the corresponding photoanode(45, 46). In addition, MoS_2 and WS_2 have been studied for application in photoelectrochemical, photovoltaic and photoelectrolysis cells(47, 48).

Finally CdS nanowire arrays and ZnS nanostructures have found applications in the field of nanogenerators, because of their ability to convert mechanical energy into electric energy by utilizing the coupling effects of their optoelectronic and piezoelectric properties(49, 50).

1.2 One dimensional nanostructures

Low-dimensional MS nanostructures find important applications in solar cells, gas sensors, light-emitting diodes, nanothermometers, piezoelectric nanogenerators, fuel cells, and lithium-ion batteries(51, 52). In particular, one-dimensional (1D) MS nanostructures are ideal for investigating the dependence of electrical transport, optical and mechanical properties on size and dimensionality (22) and are promising for the development of new generation nanodevices with high performance(53). Among their important properties stand out the lower turn-on voltage for field emitters, higher efficiency for solar cells, enhancement and better electrochemical performance for lithium-ion batteries(54, 55).

Concerning the bismuthinite family, nanowires(31, 56, 57) and nanotubes(56, 58) of Bi_2S_3, Sb_2S_3, and Sb_2Se_3 were reported. Sb_2S_3 nanowires exhibit greater ferroelectric and piezoelectric properties with respect to their bulk counterpart(59). Nanowires and nanotubes of Sb_2Se_3 show much higher conductivities than in the bulk form (56) and are promising for thermoelectric applications. Ultrathin Bi_2S_3 nanowires with diameters as small as 1.6 nm were synthesized by Cademartiri et al. (57)

The interest on semiconducting ultrathin nanostructures is becoming increasingly important for the realization of nanoscale devices(60). Carbon nanotubes (CNTs) represent a suitable choice but their separation from the synthesized mixture is challenging(61, 62). Significant attempts to synthesize ultrathin wires of silicon(8, 63) and germanium(64, 65) as well as binary(66) and ternary(67) compounds have been carried out. The main problem in the synthesis is the

ability to obtain nanostructures with homogeneous diameter. In fact, even a small tapering can causes strong fluctuations in the optoelectronic properties of the nanowires(68). There exist synthesis methods to avoid such problem, that rely on multi-step growth processes. However, they were successful mostly for diameters > 10 nm(9, 69, 70, 71). In the sub-10 nm regime, graphene nanoribbons exhibited semiconducting properties(72, 73, 74, 75, 76, 77) but to obtain homogeneous optoelectronic properties it is crucial to synthesize ribbons with clean edges and definite width(78, 79, 80, 81). Therefore, the need for a semiconducting nanostructure with well-defined size and band gap remains open. The crystalline structure of the pnictogen chalcogenides of the Bi_2S_3 family consists in an herringbone pattern of nanoribbons with a cross section of 1.1 x 0.3 nm that are aligned along a common crystallographic axis. Since the nanoribbons in the bulk are weakly bound to each other through Van der Waals forces the experimental realization of pnictogen sulfides ultrathin nanowires seems feasible. Antimonselite nanowires with diameter of 30 nm(82) and down to 20 nm have been synthesize(83). Also Sb_2Se_3 nanoribbons of 20 nm thickness(84), and nanotubes(85) of 100 nm wall thickness have been reported. 1D-nanostructures of Sb_2S_3 were synthesized as nanorods with diameters of 20 nm (86), nanoribbons and nanotubes with a thickness of 1.8 nm and 1.5 nm, respectively.(87) Also, superlattices(88) and heteroepitaxial(89) structures of Sb_2Se_3/Sb_2S_3 have been proposed. The properties of these nanostructures make them promising for several applications, such as thermoelectric, photovoltaic(90), photoconductive, and field emission devices. (91)

1.3 Pnictogen chalcogenides

Semiconducting pnictogen chalcogenides (PC) demonstrated potential applications in photovoltaic(2, 92, 93, 94) and thermoelectric devices(56). Nanostructured PC have been successfully employed to replace the inorganic dye in dye-sensitized solar cells(95), leading to a new type of cells known as solid-state semiconductor-sensitized solar cells(2, 96). Such ternary devices are based on the junction between an electron acceptor (e.g. TiO_2) a hole-transporter (e.g. a conducting polimer) and, at the interface between the two semiconductors, a

thin layer of PC nanoparticles that act as light harvester. When a photon is absorbed the nanoparticles transfer an electron to the acceptor and a hole to the hole-transporter. So far, the maximum efficiency achieved with this class of devices is 5.1%, obtained using stibnite (Sb_2S_3) as sensitizer(2). A recent compu-

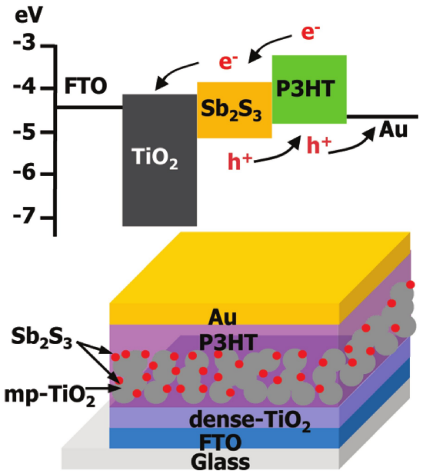

Figure 1.4: Schematic view of the solid-state semiconductor-sensitized solar cells designed by Chang et al. (2)

tational study showed that other PC, such as bismuthinite (Bi_2S_3), and guanajuatite (Bi_2Se_3), and antimonselite (Sb_2Se_3) own optical properties similar to Sb_2S_3 and therefore are, in principle, suitable sensitizers for solid-state semiconductor-sensitized solar cells. However, the authors also demonstrated that only Sb_2S_3 and Sb_2Se_3 form a type-II heterojunction with TiO_2, while Bi_2S_3 should form a type-I heterojunction that is not suitable for electron transfer to TiO_2. Some experimental studies (93, 97) are in agreement with the theoretical predictions. Further studies are therefore necessary to solve this problem.

Bi_2S_3, Sb_2S_3, Bi_2Se_3, and Sb_2Se_3 are isostructural PC that crystallize in an orthorhombic structure consisting of parallel one-dimensional $(A_4B_6)n$ ribbons, with A = Sb, Bi and B = S, Se. They are present in nature in mineral form, but several low-cost synthesis techniques have been developed as well (31, 57, 98, 99, 100, 101, 102, 103, 104). These bottom-up synthesis allows to obtain a controlled dimensionality(56, 102, 105) a good degree of crystallinity(106, 107) and the tuning the optical properties(58, 102, 108, 109). The rhombohedral phase

of Bi_2Se_3 has been largely studied topological insulator properties. However, orthorhombic Bi_2Se_3 , i.e., guanajuatite, is poorly known, since it is stable only at high temperature and pressure(110, 111). The stibnite, antimonselite, and bismuthinite band gaps have been measured extensively via optical absorption experiments. In all the cases, a wide spread in the measured gaps is reported, that is tipically attributed to the different synthesis conditions, that determine different degrees of crystallinity, different stoichiometries, and different type of defects. The measurements of the Bi_2S_3 band gaps range between 1.3-1.6 eV(112, 113, 114). while those of the Sb_2S_3 band gaps between 1.4-1.8 eV(115, 116). Antimonselite was reported with a direct gap of 1.55 eV (117) and an indirect gap between 1-1.2 eV(118).

A good number of computational studies on the bismuthinite family are also present in literature. The electronic(119, 120, 121, 122, 123, 124, 125, 126), optical and elastic (124) properties of these compounds have been already investigated. However, the inconsistencies in the calculations of band gaps and the absence of theoretical studies on low dimensional nanostructures, motivates the calculations presented in this work.

2

Theoretical and experimental methodologies

As stated in Chapter 1 the experimental data reported on bismuthinite are partly discordant. An emblematic example are the measurements of its band gap, which vary from 1.3 to 1.6 eV(112, 113, 114) depending on the synthesis procedure. The absence of photoluminescence in colloidal synthesized Bi_2S_3 nanostructures is a problem that largely hampers the investigation of their optoelectronic properties. Atomistic simulations (AS) are a valid alternative to explore the nanomaterial properties that are not accessible by experiments. In fact, even the observables that are attainable by experiments are strongly influenced by the experimental setup and the specific sample considered. AS allow one to study the intrinsic properties of a material, without all the contingent aspects that are incidental to any particular sample (impurities, vacancies, incomplete saturation, etc.). In this sense, AS can be considered as experiments on an ideal system in a controlled environment. *Ab initio* simulations (also called *first principles* simulations) take their name from the fact that they lie on a physical-mathematical theory, from which the properties of the system are derived without the use of empirical parameters. Nowadays, the density functional theory (DFT) is probably the most convenient theory to perform atomistic ab-initio simulations, due to the advantageous scalability of the computational time with the number of electrons of the system(127). The DFT is able to give a reliable prediction of the ground state

properties of a large class of materials. *Time-dependent* density functional theory (TDDFT) extends the DFT to the study of excited states of the system and the associated observables.(128)

In this chapter, a brief overview of the theoretical and experimental methods adopted in the present Thesis is reported. First, a short review on the derivation of the density functional theory is provided. Its implementation on the quantum-chemistry codes used in the Thesis (namely, QUANTUM ESPRESSO(129) and TURBOMOLE(130)) is also discussed. Concerning the experimental methods, a section is devoted to the description of synthesis and spectroscopic analysis that have been employed to validate the theoretical predictions given in this work.

2.1 Density functional theory

The density functional theory (DFT) (127) is founded on the hypothesis that a multi-electron system and all the observables associated with it can be described univocally by its density $n(\mathbf{r})$. This means that, for a system with N electrons, instead of calculating the multi-electron wavefunction $\Psi(\mathbf{R_1}, \mathbf{r_2}, \cdots, \mathbf{r_N})$ (that is a function of $3N$ variables) one can calculate the density $n(\mathbf{r})$ that has just three variables. From a practical point of view, the advantage of the DFT is linked to the fact that the computational cost of the variational procedure grows relatively slowly with the number N of electrons in the system. It can be demonstrated (127) that the computational time T follows the relationship

$$T \sim N^{\alpha} \tag{2.1}$$

with $\alpha \approx 2$ - 3.

2.1.1 The Kohn-Sham equations

Hohenberg and Kohn demonstrated (131) that it is possible to calculate the energy of the ground state of a multi-electron system by minimizing the density functional $E_v[\tilde{n}(\mathbf{r})]$ given by

$$E_v[\tilde{n}(\mathbf{r})] \equiv \min_{\alpha} \langle \tilde{\Psi}^{\alpha}_{\tilde{n}} | H | \tilde{\Psi}^{\alpha}_{\tilde{n}} \rangle \tag{2.2}$$

where $\tilde{\Psi}^{\alpha}_{\tilde{n}}$ is a trial function of the ground state with density $\tilde{n}(\mathbf{r})$.

In the case of non-interacting electrons in an external potential $v(\mathbf{r})$, the functional can be written as

$$E_v[\tilde{n}(\mathbf{r})] = \int v(\mathbf{r})\tilde{n}(\mathbf{r})d\mathbf{r} + T_s[\tilde{n}(\mathbf{r})] \tag{2.3}$$

where $T_s[\tilde{n}(\mathbf{r})]$ is a universal functional that describes the kinetic energy of a system with density $\tilde{n}(\mathbf{r})$. To find the ground state density $n(\mathbf{r})$ one needs to make the functional (2.3) stationary, i.e. to impose the condition $\delta E_v[\tilde{n}(\mathbf{r})] = 0$:

$$\delta E_v[\tilde{n}(\mathbf{r})] = \int \delta\tilde{n}(\mathbf{r}) \left\{ v(\mathbf{r}) + \frac{\delta}{\delta\tilde{n}(\mathbf{r})} T_s[\tilde{n}(\mathbf{r})]|_{\tilde{n}(\mathbf{r})=n(\mathbf{r})} - \epsilon \right\} d\mathbf{r} = 0 \tag{2.4}$$

where ϵ is the Lagrange multiplier. The solution of the Eq. (2.4) is known: the ground state energy E and density $n(\mathbf{r})$ of a system composed by non-interacting particles can be determined by means of the Schroedinger equations

$$\left\{ -\frac{1}{2}\nabla^2 + v(\mathbf{r}) \right\} \phi_j(\mathbf{r}) = \epsilon_j \phi_j(\mathbf{r}) \tag{2.5}$$

that give

$$E = \sum_{j=1}^{N} \epsilon_j \tag{2.6}$$

$$n(\mathbf{r}) = \sum_{j=1}^{N} |\phi_j(\mathbf{r})|^2 \tag{2.7}$$

Let us consider now a system of interacting particles. In this case, the density functional $E_v[\tilde{n}(\mathbf{r})]$ can be written as

$$E_v[\tilde{n}(\mathbf{r})] = \int v(\mathbf{r})\tilde{n}(\mathbf{r})d\mathbf{r} + F[\tilde{n}(\mathbf{r})] \tag{2.8}$$

where

$$F[\tilde{n}(\mathbf{r})] \equiv T_s[\tilde{n}(\mathbf{r})] + \frac{1}{2}\int \frac{n(\mathbf{r})n(\mathbf{r}')}{|\mathbf{r}-\mathbf{r}'|} d\mathbf{r}d\mathbf{r}' + E_{xc}[\tilde{n}(\mathbf{r})] \tag{2.9}$$

The second term of the right-hand side is the Hartree interaction, while $E_{xc}[\tilde{n}(\mathbf{r})]$ is the so called *exchange-correlation functional*, that contains all the energy cor-

rections that are not included in the Hartree term. Again, to find the ground state density $n(\mathbf{r})$ one needs to impose the condition $\delta E_v[\tilde{n}(\mathbf{r})] = 0$, i.e

$$\delta E_v[\tilde{n}(\mathbf{r})] = \int \delta\tilde{n}(\mathbf{r}) \left\{ v_{eff}(\mathbf{r}) + \frac{\delta}{\delta\tilde{n}(\mathbf{r})} T_s[\tilde{n}(\mathbf{r})]|_{\tilde{n}(\mathbf{r})=n(\mathbf{r})} - \epsilon \right\} d\mathbf{r} = 0 \tag{2.10}$$

where

$$v_{eff}(\mathbf{r}) = v(\mathbf{r}) + \int \frac{n(\mathbf{r}')}{|\mathbf{r} - \mathbf{r}'|} d\mathbf{r}' + v_{xc}(\mathbf{r}) \tag{2.11}$$

and

$$v_{xc}(\mathbf{r}) = \frac{\delta}{\delta\tilde{n}(\mathbf{r})} E_{xc}[\tilde{n}(\mathbf{r})]|_{\tilde{n}(\mathbf{r})=n(\mathbf{r})} \tag{2.12}$$

$v_{xc}(\mathbf{r})$ is called *exchange-correlation potential*. Since Eqs. (2.10) and (2.4) have the same form, the single particle equations for the interacting case are given by

$$\left\{ -\frac{1}{2}\nabla^2 + v_{eff}(\mathbf{r}) \right\} \phi_j(\mathbf{r}) = \epsilon_j \phi_j(\mathbf{r}) \tag{2.13}$$

and are called *Kohn-Sham equations* (KS). By iterative self-consistent solution of the KS eqs. one obtains the energy and the density of the ground state of the interacting system:

$$E = \sum_{j=1}^{N} \epsilon_j + E_{xc}[n(\mathbf{r})] - \int v_{xc}(\mathbf{r}) n(\mathbf{r}') d\mathbf{r}' - \frac{1}{2} \int \frac{n(\mathbf{r}) n(\mathbf{r}')}{|\mathbf{r} - \mathbf{r}'|} d\mathbf{r} d\mathbf{r}' \tag{2.14}$$

$$n(\mathbf{r}) = \sum_{j=1}^{N} |\phi_j(\mathbf{r})|^2 \tag{2.15}$$

The difficulty in finding the self-consistent solution of the KS equations is disguised in the exchange-correlation term $E_{xc}[\tilde{n}(\mathbf{r})]$ which is actually unknown. In principle, if one were able to determine $E_{xc}[\tilde{n}(\mathbf{r})]$ exactly, the KS equations would include all the many-body effects. However, the complexity of the multi-electrons interaction prevents an exact solution and approximations needs to be adopted to solve the problem.

2.1.2 Exchange-correlation energy approximations

For many materials (especially metals), the screening effect on a reference electron exerted by the other electrons is sufficient to screen it completely on a distance of about the Fermi wavelength $\lambda_F(r) = [3\pi n(r)]^{-1/3}$. This means that a reference electron does not *feel* the charge distribution for distances longer than λ_F (the so called *nearsightedness* of the electron). Hence, its exchange-correlation (XC) energy depends only on the charge distribution $n(\mathbf{r})$ in its proximity. These considerations are the foundations of the *quasi-local approximation* (QLA) for the XC energy $E_{xc}[n(\mathbf{r})]$:

$$E_{xc}[n(\mathbf{r})] = \int e_{xc}(\mathbf{r}, [n(\tilde{\mathbf{r}})])n(\mathbf{r})d\mathbf{r} \tag{2.16}$$

where e_{xc} is the one-electron XC energy. The approximation is *quasi-local* because e_{xc} in $\mathbf{r}$ depends only on the charge distribution in $\tilde{\mathbf{r}}$, where $\tilde{\mathbf{r}}$ differs from $\mathbf{r}$ for a small distance of the order of λ_F.

The QLA can be implemented in a code for atomistic simulations in different ways. The *local density approximation* (LDA) assumes that the one electron XC energy e_{xc} in $\mathbf{r}$ with density $n(\mathbf{r})$ is that of a uniform gas of electrons with density $n(\mathbf{r})$:

$$E_{xc}^{LDA}[n(\mathbf{r})] = \int e_{xc}(\mathbf{r}, n(\mathbf{r}))n(\mathbf{r})d\mathbf{r} \tag{2.17}$$

In the case of a uniform gas of electrons the XC energy can be considered as the sum the exchange energy and the correlation energy ($e_{xc} = e_x + e_c$), which are given by

$$e_x(n) = -\frac{0,458}{r_s} \tag{2.18}$$

$$e_c(n) = -\frac{0,44}{r_s + 7,8} \tag{2.19}$$

where r_s is the radius of the average sphere of volume occupied by each electron. When the density is not uniform the Eqs. (2.18) and (2.19) can still be adopted with a variable $r_s(\mathbf{r})$.

A more accurate estimate of the XC energy is given by the *generalized gradient approximation* (GGA). In this case, e_{xc} depends not only on $n(\mathbf{r})$ but also on the

gradient of the density, $\nabla n(\mathbf{r})$:

$$E_{xc}^{GGA}[n(\mathbf{r}); \nabla n(\mathbf{r})] = \int e_{xc}^{(1)}(\mathbf{r}, n(\mathbf{r}), \nabla n(\mathbf{r})) n(\mathbf{r}) d\mathbf{r} \tag{2.20}$$

The E_{xc}^{GGA} functional has been implemented in several ways, with different accuracy and computational cost. Among the most widespread implementations, we mention the Vosko-Wilk-Nusair (1980) functional, the Lee-Yang-Parr (1988) functional, and the Perdew-Burke-Ernzerhof (1996) functional. (132)

In 1993 A. Becke introduced the idea to calculate the XC energy with a so called *hybrid functional*. (133) Hybrid functionals incorporate a portion of *exact* exchange from the Hartree-Fock theory with the *approximate* exchange and correlation estimated using LDA, GGA, etc. The exact exchange functional is expressed in terms of KS orbitals rather than the density and, for this reason, it is also referred as *implicit density functional*. The hybridization allows to improve the estimation of several chemical-physical properties, including the atomization energy and the bond lengths. The B3LYP functional (short for Becke 3-parameter Lee-Yang-Parr) (134) is one of the most famous hybrid functionals and was also adopted in some simulations of finite systems in the present Thesis.

2.2 Excited states

2.2.1 Time-dependent DFT

The DFT is a ground state theory, i.e. the KS equations are in principle inadequate to compute the energy of an excited state. Time-dependent density functional theory (TDDFT) is an extension of DFT that is suitable to investigate the properties and dynamics of multi-electron systems in the presence of time-dependent potentials (i.e. excited states). Through TDDFT it is possible to calculate excitation energies, frequency-dependent response properties, and photoabsorption spectra.

Similarly to DFT, TDDFT is based on the fundamental hypothesis that the *time-dependent* wave function can be replaced by the time-dependent electronic density to derive the effective potential of a fictitious non-interacting system

which returns the same density as any given interacting system. Since the time-dependent effective potential at any given instant depends on the value of the density at all the previous instants, the construction of the fictitious non-interacting system is more complex in TDDFT than in DFT. This fact cause a large increment of the computational cost needed to perform atomistic calculations on excited states.

The formal foundation of TDDFT is the Runge-Gross (RG) theorem (1984)(128), the time-dependent analogue of the Hohenberg-Kohn (HK) theorem (1964).(131) The RG theorem shows that, for a given initial wave function, there is a unique mapping between the time-dependent external potential of a system and its time-dependent density. This implies that the many-body wave function, depending upon 3N variables, is equivalent to the density, which depends upon only 3, and that all properties of a system can thus be determined from knowledge of the density alone. Unlike in DFT, there is no general minimization principle in time-dependent quantum mechanics. Consequently the proof of the RG theorem is more involved than the HK theorem. Given the RG theorem, the next step in developing a computationally useful method is to determine the fictitious non-interacting system which has the same density as the physical (interacting) system of interest. As in DFT, this is called the (time-dependent) Kohn-Sham system. This system is formally found as the stationary point of an action functional defined in the Keldysh formalism.(135) The most popular application of TDDFT is in the calculation of the energies of excited states of isolated systems and, less commonly, solids. Such calculations are based on the fact that the linear response function (i.e. how the electron density changes when the external potential changes) has poles at the exact excitation energies of a system. Such calculations require, in addition to the exchange-correlation potential, the exchange-correlation kernel, i.e. the functional derivative of the exchange-correlation potential with respect to the density.(136)

2.2.2 Delta self-consistent field method

While Density Functional Theory (DFT) has been successfully applied to obtain the ground state electronic properties of a large class of materials, it is well rec-

ognized that the use of Kohn-Sham eigenvalues to determine the quasi-particle properties of many-electrons systems yields, by and large, results in disagreement with experiments (137). For example, the well-known band-gap problem for bulk semiconductors arises from a severe underestimate (even exceeding 50%) of the electronic excitation energies with respect to available experimental results (optical absorption, direct and inverse photo-emission) (138). In optical absorption experiments, in particular, an electron excited into a conduction state interacts with the resulting hole in the previously occupied state and two-particles (excitonic) effects must be properly considered (138).

For finite systems it is possible to obtain accurate excitation energies using the so-called delta-self-consistent-field (ΔSCF) approach (137, 138). This method, successfully applied to obtain the quasi-particle energies for several clusters and isolated molecules (139), consists in evaluating total energy differences between the self-consistent calculations performed for the system with N and N$\pm$1 electrons, respectively.

At the optimized geometry of the neutral system in the present work we have evaluated the vertical electron affinity (EA_v) and the vertical first ionization energy (IE_v). This enabled the calculation of the quasiparticle-corrected HOMO-LUMO gap of the neutral systems; this quantity is usually referred to as the fundamental energy gap and is rigorously defined within the ΔSCF scheme (140) as:

$$QP^1_{gap} = IE_v - EA_v = E_{N+1} + E_{N-1} - 2E_N, \tag{2.21}$$

E_N being the total energy of the N-electron system.

In the framework of ΔSCF it is also possible to use the following approximate expression:

$$QP^2_{gap} = \epsilon^{N+1}_{N+1} - \epsilon^N_N, \tag{2.22}$$

where ϵ^j_i is the i^{th} Kohn-Sham eigenvalue of the j-electron system. The results obtained using the above Eqs. (2.21) and (2.22) tend to coincide as the system gets larger and the orbitals more delocalized.

2.3 Atomistic simulation softwares

To perform the ab initio simulations of the present Thesis, two quantum-chemistry codes were used: Turbomole and Quantum Espresso.

Turbomole is a highly optimized software package for large-scale quantum chemical simulations of molecules, clusters, and periodic solids. It adopts a Gaussian basis sets. The principal advantage of Gaussian-type orbitals (GTOs) in

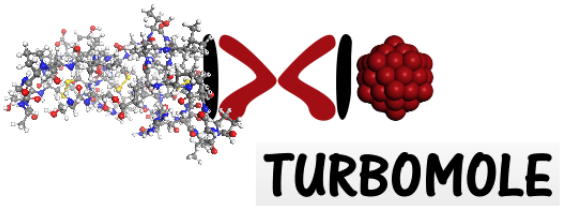

Figure 2.1: The logo of Turbomole.

molecular quantum chemical calculations is that the *Gaussian Product Theorem* guarantees that the product of two GTOs centered on two different atoms is a finite sum of Gaussians centered on a point along the axis connecting them. In this manner, four-center integrals can be reduced to finite sums of two-center integrals, and in a next step to finite sums of one-center integrals. The speed-up by 4-5 orders of magnitude compared to Slater orbitals more than outweighs the extra cost entailed by the larger number of basis functions generally required in a Gaussian calculation. Turbomole specializes on predictive electronic structure methods with excellent cost to performance characteristics, such as (time-dependent) density functional theory (TDDFT), second-order Moller-Plesset theory, and explicitly correlated coupled cluster (CC) methods. These methods are combined with ultraefficient and numerically stable algorithms such as integral-direct and Laplace transform methods, resolution-of-the-identity, pair natural orbitals, fast multipole, and low-order scaling techniques. Apart from energies and structures, a variety of optical, electric, and magnetic properties are accessible from analytical energy derivatives for electronic ground and excited states.

Quantum Espresso (QE) is an integrated suite of computer codes for electronic-structure calculations and materials modeling, based on density-functional theory,

plane waves, and pseudopotentials (norm-conserving, ultrasoft, and projector-augmented wave). The plane-wave (PW) basis set is convenient because with

Figure 2.2: The logo of Quantum Espresso.

periodic boundary conditions some integrals and operations are much easier to code and carry out with PW basis functions than with their localized counterparts. PW basis sets are used to describe the valence charge density while the core electrons are described by means of pseudopotentials. This is because core electrons tend to stay close to the atomic nuclei, resulting in large wave function and density gradients near to the nuclei which are not easily described by a PW basis set unless a very high energy cutoff is used (drastically increasing the computational cost of the simulation). Using Fast Fourier Transforms, one can work with PW basis sets in reciprocal space in which integrals and derivatives are computationally less demanding to be carried out. Another important advantage of a PW basis is that it is guaranteed to converge in a smooth, monotonic manner to the target wavefunction, while there is only a guarantee of monotonic convergence for all Gaussian-type basis sets when used in variational calculations. The acronym *ESPRESSO* stands for opEn Source Package for Research in Electronic Structure, Simulation, and Optimization. It is freely available to researchers under the terms of the GNU General Public License. High serial performance across different architectures is achieved by the systematic use of standardized mathematical libraries (BLAS, LAPACK, and FFTW) for which highly optimized implementations exist on many platforms; when proprietary optimizations of these libraries are not available, the user can compile the library sources distributed with QE. Optimal performance in parallel execution is achieved through the design of several parallelization levels, using sophisticated communication algorithms, whose implementation often does not need to concern the developer, being embedded and concealed in appropriate software layers. As a result the performance of the

key engines, PWscf and CP, may scale efficiently on massively parallel computers up to thousands of processors.

2.4 Experimental techniques

Although mostly theoretical, the present work includes also an experimental investigation on the synthesis and spectroscopic characterization of bismuth sulfide nanostructures. The experiments are useful to verify the validity of the computational predictions on the Bi_2S_3 nanocrystals.

The syntheses are performed using a low-cost non-toxic colloidal technique. Colloidal synthesis of quantum dots is done by using precursors, organic surfactants, and solvents. Heating the solution, the precursors decompose forming

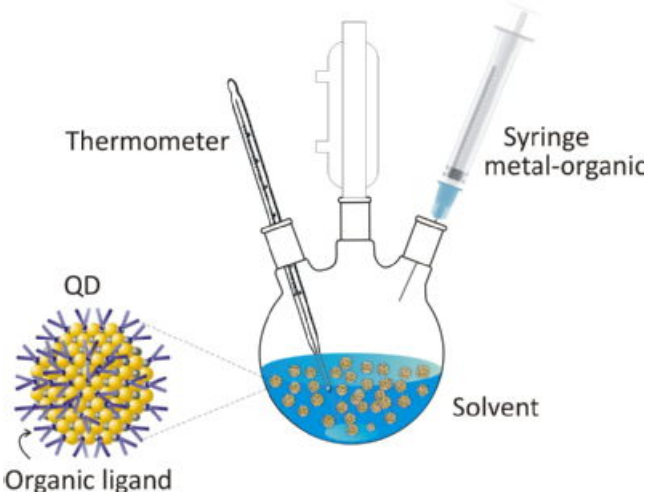

Figure 2.3: Representation of the experimental apparatus employed in the preparation of colloidal quantum dots. (3)

monomers which then nucleate and generate nanocrystals. The temperature during the synthesis process is a critical factor in determining optimal conditions for the nanocrystal growth. It must be high enough to allow for rearrangement and annealing of atoms during the synthesis process while being low enough to promote crystal growth. The concentration of monomers is another critical factor that has to be stringently controlled during nanocrystal growth. The growth

process of nanocrystals can occur in two different regimes, "focusing" and "defocusing". At high monomer concentrations, the critical size (the size where nanocrystals neither grow nor shrink) is relatively small, resulting in growth of nearly all particles. In this regime, smaller particles grow faster than large ones (since larger crystals need more atoms to grow than small crystals) resulting in "focusing" of the size distribution to yield nearly monodisperse particles. The size focusing is optimal when the monomer concentration is kept such that the average nanocrystal size present is always slightly larger than the critical size. Over time, the monomer concentration diminishes, the critical size becomes larger than the average size present, and the distribution "defocuses". There are colloidal methods to produce many different semiconductors. Typical dots are made of binary compounds such as lead sulfide, lead selenide, cadmium selenide, cadmium sulfide, indium arsenide, and indium phosphide. Dots may also be made from ternary compounds such as cadmium selenide sulfide. These quantum dots can contain as few as 100 to 100,000 atoms within the quantum dot volume, with a diameter of 10 to 50 atoms. This corresponds to about 2 to 10 nanometers, and at 10 nm in diameter, nearly 3 million quantum dots could be lined up end to end and fit within the width of a human thumb.

The phase and stoichiometry of the synthesized Bi_2S_3 nanocrystals are analyzed by means of X-ray diffraction (XRD). Since the sample is nanostructured, the appropriate instrument for the XRD analysis is the powder diffractometer. The nanocrystalline sample is placed into a goniometer and bombarded with a finely focused monochromatic beam of X-rays, producing a diffraction pattern. Ideally, every possible crystalline orientation is represented equally in a powdered sample. The resulting orientational averaging causes the three-dimensional reciprocal space that is studied in single crystal diffraction to be projected onto a single dimension. When the scattered radiation is collected on a flat plate detector, the rotational averaging leads to smooth diffraction rings around the beam axis, rather than the discrete Laue spots observed in single crystal diffraction. The angle between the beam axis and the ring is called the scattering angle and in X-ray crystallography is always denoted as 2θ (in scattering of visible light the convention is usually to call it θ). In accordance with Bragg's law, each ring corresponds to a particular reciprocal lattice vector in the sample crystal. Powder

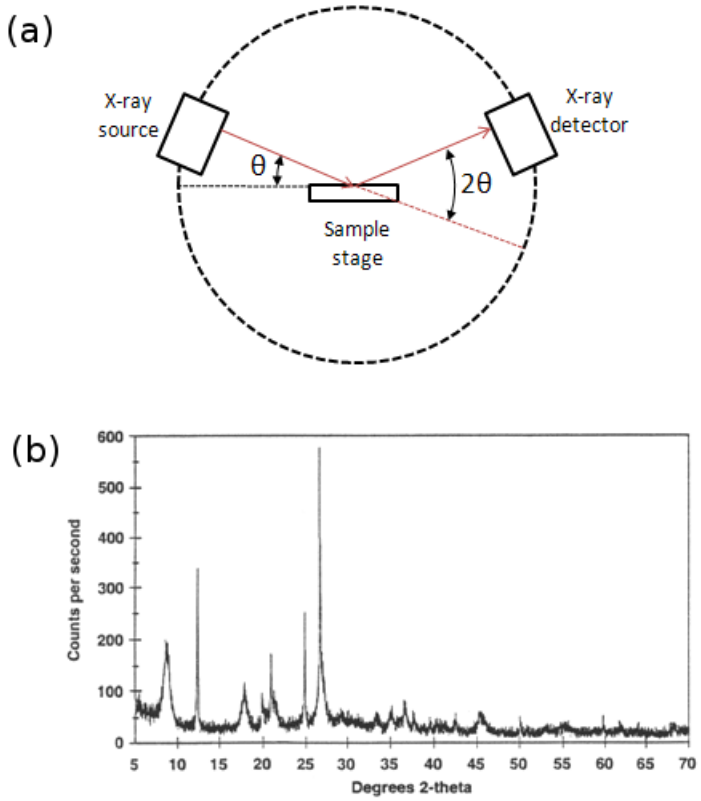

Figure 2.4: (a) Schematic representation of a powder diffractometer(4); (b) X-ray powder diffractogram. Peak positions occur where the X-ray beam has been diffracted by the crystal lattice. The unique set of d-spacings derived from this patter can be used to "fingerprint" the mineral. (5)

diffraction data are usually presented as a diffractogram in which the diffracted intensity, I, is shown as a function either of the scattering angle 2θ or as a function of the scattering vector length q.

The optoelecronic properties of the Bi_2S_3 nanocrystals are studied using the pump-probe spectroscopy. Such technique enables to follow in real time the carrier dynamics during an electronic transition. In a pump-probe experiment the output pulse train from an ultrafast laser, is divided into two beams: the sample is excited by one pulse train (pump) and the changes it induces in the sample are probed by the second pulse train (probe), which is suitably delayed

with respect to the pump. Some properties related to the probe (reflectivity, absorption, luminescence, Raman scattering) are then monitored to investigate the changes produced by the pump in the sample. The simplest of the pump-probe spectroscopy experiments is the measurement of the transmitted probe. In this case, one generally measures the change in the transmitted probe pulse energy induced by the pump as a function of the time delay between the pump and the probe pulses.

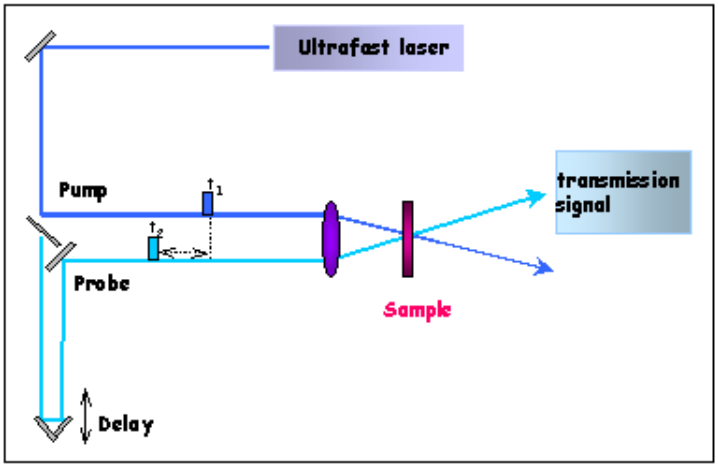

Figure 2.5: Schematic representation of the experimental setup employed in pump-probe spectroscopy. (6)

3

Bismuth sulfide structure and properties

In the present Chapter the structural and electronic properties of the bulk Bi_2S_3 are investigated. The atomic relaxation of the Bi_2S_3 crystal structure was studied by means of DFT-GGA simulations and compared to previous data present in literature. Also, its electronic band structure, density of states, and charge density are investigated. Finally, the effect of bismuth and sulfur vacancies was explored. This study is a preliminar step to the investigation of Bi_2S_3 nanostructures reported in the next chapter.

3.1 Crystal structure

Bismuth sulfide (Bi_2S_3) is a layered semiconductor that crystallizes in the orthorhombic system. It belongs to the *Pnma* space group (or the equivalent *Pbnm* space group) and is isostructural to stibnite (Sb_2S_3) and antimonselite (Sb_2Se_3) (141). The structure of Bi_2S_3 at ambient conditions was originally determined by Kupčik and Veselá Nováková (142) and re-refined by Kyono and Kimata (143).

Bi_2S_3 has a strongly anisotropic crystal structure (see Fig. 3.1), consisting in an herringbone pattern of nanoribbons extending along the y-direction (*Pnma*) or the z-direction (*Pbnm*), according to the considered notation. Unless differently declared, the adopted notation in this and the following chapters is the

Method	a	b	c	Ref.
Exp.	11.269	3.9717	11.129	(144)
LDA	11.030	3.949	10.853	(145)
GGA	11.597	3.9706	11.041	Calzia et al. (submitted)

Table 3.1: Bi_2S_3 lattice parameters. All values in angstrom.

Pnma. The unit cell contains four Bi_2S_3 units (20 atoms) belonging to the two

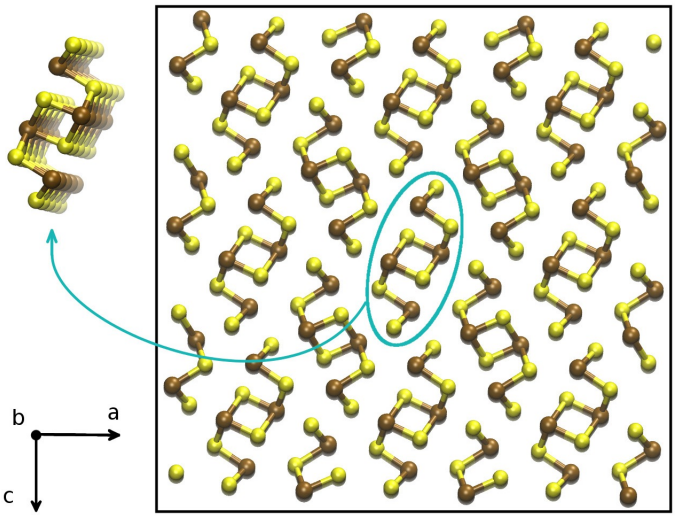

Figure 3.1: Crystal structure of Bi_2S_3 (S atoms in yellow, Bi atoms in brown). The bulk consists in an herringbone pattern of ribbons (see single ribbon in the inset) extending along the [010] direction.

inequivalent ribbons that define the crystal structure. An experimental study by Lundegaard et al. (144) provides high quality data about lattice parameters and atomic positions of Bi_2S_3. We adopt such data as starting geometry for our simulation cell and then relax both the lattice constants and the atomic positions. Table 3.1 compares our results with experimental data and other theoretical data. It can be observed that the generalized gradient approximation (GGA) (implemented with the Perdew-Ernzerhof-Burke (PBE) functional) provides a better agreement with experimental data, with respect to the local density approximation (LDA). In particular, the lattice parameter along the y-direction

is substantially unchanged, while a small expansion of 2.9% and a contraction of 0.8% is observed along the x and z-direction, respectively.

A peculiarity of bismuth sulfide and other pnictogen sulfides of the same family (such as Sb_2S_3) is the different types of forces that characterize its crystal structure. The stability of the single ribbon is dictated by covalent/ionic bonds between the bismuth and the sulfur atoms that compose it. On the other hand, the inter-ribbon interaction is mostly due to van der Waals forces(120, 144) with a weak contribution due to electronic interaction. We will better explore this interaction in the next chapter (where a single ribbon model and several kind of nanostructures are proposed) but we already bring forward a couple of evidences here.

First evidence is obtained by calculating the total energy of the single ribbon against that of the bulk. The total energy difference between the two systems demonstrates that the inter-ribbon interaction is smaller than 0.2 eV/atom, to be compared with the large binding energy (2-3 eV/atom) within the atoms of the same ribbon due to the strong Bi-S chemical bonds. Another aspect that underlines the small interaction between the ribbons is obtained by calculating the band structure of the bulk (see section 3.2). As it will be shown, the small dispersion of the bands in the directions perpendicular to the ribbon axis is a manifestation of the weak inter-ribbon electronic interaction.

It should be observed that the current van der Waals density functionals (146, 147) (VDW-DFs) implemented in QUANTUM ESPRESSO and other simulation codes produce a worse agreement with the experimental data with respect to the plain GGA-PBE exchange-correlation functional. In particular, the lattice constant along the ribbon axis is overestimated of about the 2% with respect to the experiments, to be compared with an accuracy of about the 0.1% obtained by using the GGA-PBE functional. For this reason most of the calculations has been performed without the use of van der Waals contribution.

3.2 Electronic properties

In Fig. 3.2 the band structure of the bulk Bi_2S_3 is reported. In good agreement with the experiments, we observe a band gap of 1.4 eV. The gap is direct and

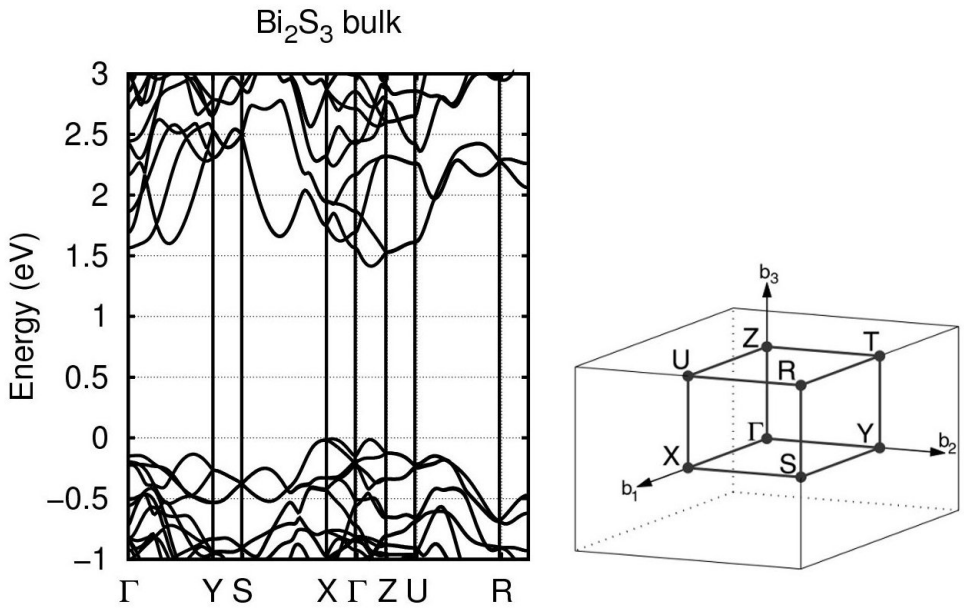

Figure 3.2: Left: band structure of the bulk Bi_2S_3 in the *Pnma* notation. The zero of the energy scale correspond to the top of the valence band. Right: high-simmetry directions for an orthorhombic crystal.

located between the Γ and Z points. It is relevant to note that the agreement between the calculations and the experiments on the amplitude of the band gap is in part fortuitous, since it comes from the cancellation between spin-orbit and quasiparticle effects (119) (here not considered). The band dispersion and the position of the band gap in the Brillouin zone (BZ) are in agreement with those obtained by Larson et al. in a previous theoretical study(122) (be aware that Larson used the *Pbnm* notation instead of the *Pnma*.). By focusing on the conduction bands (CBs), we observe a large dispersion along the directions of the reciprocal space that are parallel to the ribbon axis, i.e. $\Gamma - Y$, $S - X$, and $U - R$. This is consistent with a stronger interaction and an higher electron mobility along the ribbon with respect to the plane perpendicular to it. Concerning the electron mobility, we calculated the effective mass of the electron along the x, y and z-direction with respect to the CB minimum of the band gap. We obtained the following results (normalized to the free electron mass m_e): $m_x^*/m_e = 3.4$, $m_y^*/m_e = 0.8$, $m_z^*/m_e = 2.1$ These data confirm a higher mobility and a larger electronic coupling along the ribbon axis. As for the inter-ribbon interaction in

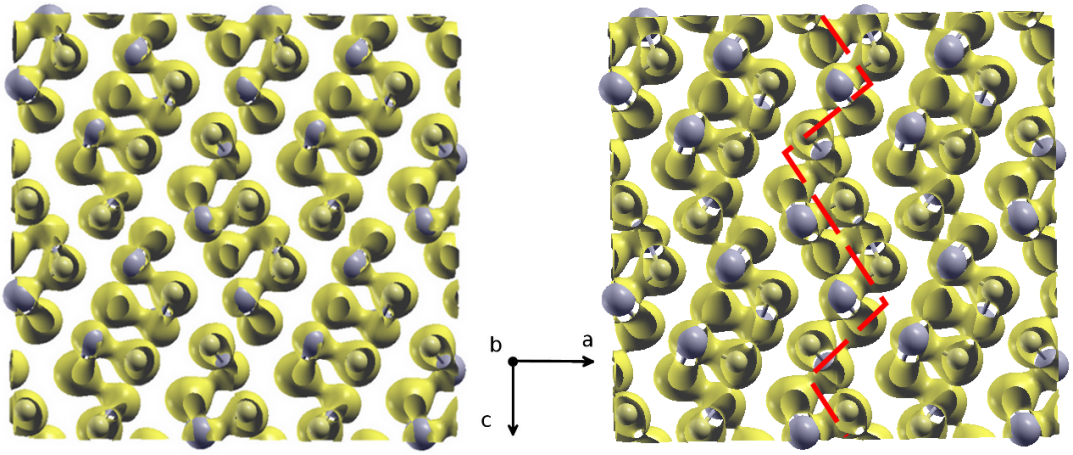

Figure 3.3: Charge density isosurfaces (yellow clouds) of the bulk Bi_2S_3. Left: $4 \cdot 10^{-2}$ e^- Bohr^{-3} isosurface. Right: $3 \cdot 10^{-2}$ e^- Bohr^{-3} isosurface. The red dashed line highlights the formation of interacting stripes of ribbons along the z-direction.

the x-z plane, the lower value of m_z^* with respect to m_x^* suggests a preferential coupling along the z-direction. Such anisotropy is explained by analyzing the charge density (CD) of the system (see Fig. 3.3). For isosurfaces down to $4 \cdot 10^{-2}$ e$^-$ Bohr^{-3} (left panel) there is no overlap between the electronic clouds of the single ribbons. For lower values (right panel) a small interaction begins to that place along the z-direction, while no interaction is observed along the x-direction. This fact is in agreement with the result $m_x^* > m_z^*$ and indicates smaller mobility of the electrons along the x-direction.

In Fig. 3.4 the density of state (DOS) of the bulk Bi_2S_3 is reported. The decomposition of the DOS in its bismuth and sulfur contribution (bottom panel) reveals a predominance of the sulfur component for the valence states, and an almost equal contribution of the sulfur and bismuth components for what concerns the conduction states.

3.3 Defects

Many experimental studies, especially those concerning colloidal samples, report the absence of photoluminescence in Bi_2S_3 (19). Also, as cited above, the experimental data concerning the Bi_2S_3 band gap are quite scattered, ranging from 1.2

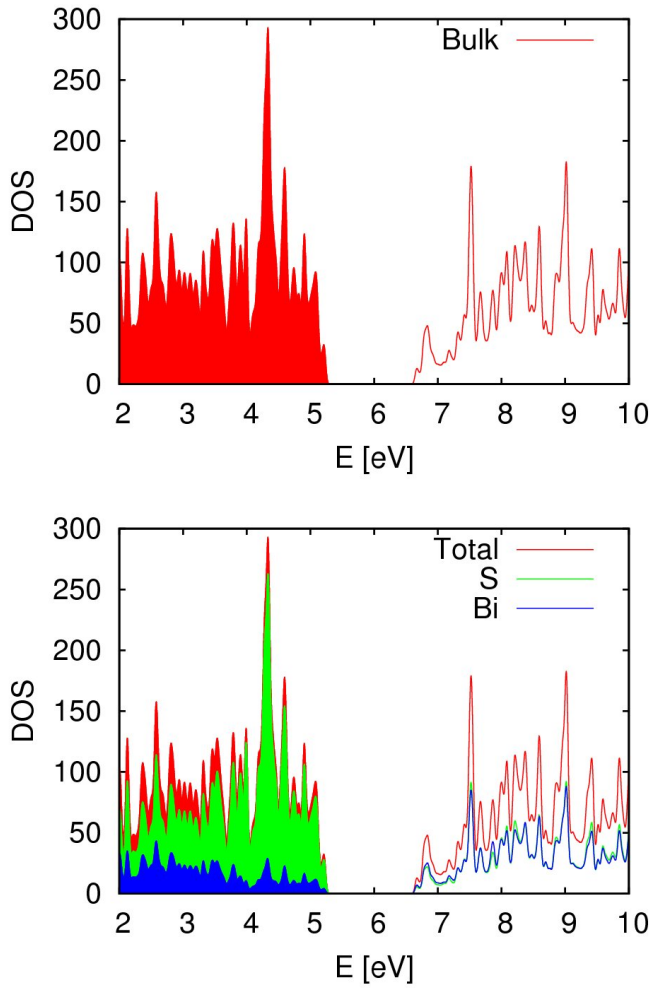

Figure 3.4: Density of state (DOS) of the bulk Bi_2S_3. The top panel reports the total DOS while the bottom panel decomposes the DOS in the contribution of the bismuth and sulfur atoms. In both panels, occupied states are represented by filled curve, while empty states appear as empty curve.

to 1.7 eV. These aspects have been related to the presence of intra-gap states. The appearance of such states is due to two distints issues. First, low-temperature in-solution synthesis techniques (such as colloidal method), though cheaper than high-temperature in-vacuo methods, do not allow a perfect control over the stoichiometry and crystallinity of the product. In addition, Bi_2S_3 reveals a low *defect tolerance*, which means that even a low density of defects tends to accumulate

energy states inside the band gap, i.e. deep trap states that ruin the optoelectronic properties of the crystal. We focused our study on the effects of bismuth

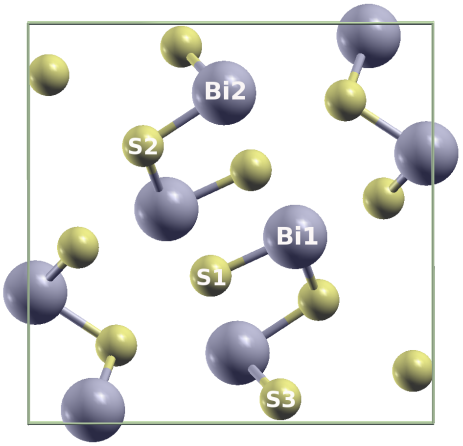

Figure 3.5: The unit cell of Bi_2S_3 contains 20 atoms. However, using the symmetries of the *Pnma* space group, it can be built just by five inequivalent atoms (the so called *asymmetric unit*).

and sulfur vacancies on the electronic stucture of bismuthinite. With this aim, we built a 2x3x2 supercell of Bi_2S_3 (240 atoms) and performed five indipendent DFT calculations removing each time one of the five inequivalent atoms of the crystal structure (see Fig. 3.5). The results show that all the sulfur atoms generate doubly occupied states that lie deep in the band gap (0.8 eV above the VB, 0.6 eV below the CB) while the bismuth vacancies generate half-empty states a few tens of meV above the VB. The substantial agreement of our results with previous studies (148) suggests that the sulfur vacancies are likely responsible for the absence of photoluminescence in several experimental investigation on Bi_2S_3.

3.4 Methodological details

All the calculations were performed with the QUANTUM ESPRESSO code(129). The initial geometry was chosen corresponding to the experimental data reported by Lundegaard et al.(144) The Perdew-Burke-Ernzerhof (PBE)(132) was used to perform geometry optimizations. The valence electron wave functions were expanded in planewaves basis sets with kinetic energy cutoff of 30 Ry. Valence

electrons were explicitly described, while the core-valence interaction was taken into account by means of Troullier-Martins pseudopotentials.(149) The reciprocal space was sampled with a (8x8x8) Brillouin zone mesh centered at Γ.

4

Nanostructures of Bi_2S_3

The unit cell of pnictogen sulfides such as Bi_2S_3 or Sb_2S_3 is characterized by a relatively high number of atoms. On the other hand, the intrinsic anisotropy of their crystal structure allows us to look at the bulk as a herringbone pattern of parallel ribbons that loosely interact with each other by means of dispersive forces. The twofold nature of strong intra-ribbon versus weak inter-ribbon forces, suggests the legitimacy to study *some* morphologic and electronic properties of the bulk by means of a single ribbon model. In section 1.2 the modern relevance of semiconducting 1D nanostructures in several fields of science and engineering was introduced. Due to their anisotropic structure, pnictogen sulfides are excellent candidates for this purpose. Bi_2S_3 is mostly synthesized in form of elongated nanostructures (nanorods(19, 150, 151, 152, 153, 154, 155) or nanowires(57, 152, 156, 157, 158)) that extends along the ribbon axis. In these type of structures, one is naturally interested to study mechanical and optoelectronic properties that concern primarily the ribbon structure. The first study to propose the single ribbon model was published by Vadapoo et al (121). They proposed it to study the stability of Sb_2S_3 and Sb_2Se_3 nanostructures, their quantum confinement effect and the behaviour of heterostrucures between the two materials.

In this Chapter, the single ribbon model is used to study the morphologic and optoelectronic properties of Bi_2S_3,(19, 159) The study starts from the calculation of the properties of an isolated ribbon periodically repeated along its main axis. Then, saturated and unsaturated nanoribbons of finite size are considered. By means of DFT calculations and experimental techniques, evidence that the opti-

cal gap can be tuned through quantum confinement is provided. By a comparison with Sb_2S_3, it is possible to conclude that Bi_2S_3 nanostructures have similar tunability of the band gap and a better tendency of passivating defects at the (010) surfaces through local reconstructions. In Section 4.3, the study of ultrathin nanowires (NWs) obtained by the aggregation of more than one nanoribbon is presented. It is shown that crystalline NWs consisting of more than 7-9 nanoribbons are expected to be stable structures at room temperature. In line with the theoretical analysis, ultrathin Bi_2S_3 NWs that extend along the [010] crystallographic direction have been synthesized with a coherence length of around 30 nm. To do this, a novel oleylamine based organometallic synthesis employing bismuth acetate as precursor have been used. The electronic properties of the ultrathin Bi_2S_3 nanowires are further investigated within the framework of density functional theory (DFT) to study intra-gap states and passivation strategies by organic molecules.

4.1 Periodic nanoribbon

A single ribbon was extracted from the bulk structure. Periodic boundaries conditions were applied along the ribbon axis, so that the system is an infinite one-dimensional nanostructure. Relaxation shows a minor geometry optimization effect, consisting in a slight re-orientation of bonds along the ribbon axis (see Fig. 4.1).

A small expansion of about 2% in the (010)-plane is also observed. Consistently with the weak electronic coupling between ribbons found in experiments(144, 160) and previous theoretical works(120, 123), the calculations show a small cohesive energy difference between the ribbon and the bulk. In particular the total energy difference is smaller than 0.2 eV/atom to be compared with the large binding energy (2-3 eV/atom) within the atoms of the same ribbon due to the strong Bi-S chemical bonds. The results also show that the band gap of the single ribbon relaxed in vacuo is 0.1 eV higher than the band gap of the relaxed Bi_2S_3 bulk (1.5 eV vs. 1.4 eV). This proves that, consistently with the weak electronic coupling between ribbons, there is only a slight dependence of the electronic gap on the size of the system in the (010)-plane. This is also consistent with theoret-

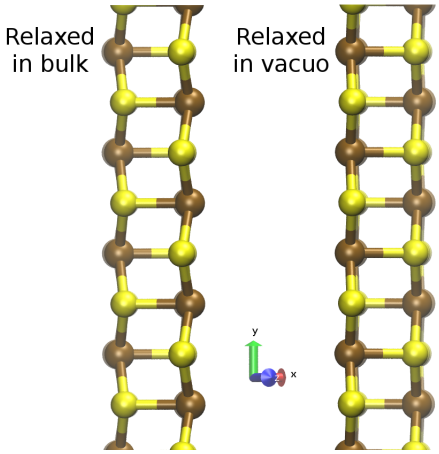

Figure 4.1: A comparison between the optimized geometry of a Bi_2S_3 ribbon relaxed inside the bulk (left) and a Bi_2S_3 ribbon relaxed in vacuo (right).

ical results(121) for Sb_2S_3. Conversely, in the next sections it will be shown that the electronic confinement is sizable in the direction parallel to the ribbon axis.

4.2 Finite length nanoribbons

Bi_2S_3 single ribbons of variable size within the range 1-10 nm have been considered by properly cutting the infinite ribbon along the (010)-plane. This gives rise to two surfaces and ten dangling bonds for each ribbon-like nanocrystal. The first step is to perform self-consistent field DFT calculations at fixed atomic positions with the PBE exchange-correlation functional. The (010)-surfaces give rise to surface states that lie within the fundamental gap. The corresponding HOMO-LUMO gap (HOMO: Highest Occupied Molecular Orbital; LUMO: Lowest Unoccupied Molecular Orbital) turns out to be as small as 0.3-0.5 eV in all cases. In fact, by inspecting the energy position of the molecular orbitals in Fig. 4.2(a) and their spatial extension in Fig. 4.3 it was observed that for each ribbon there are ten surface states (six occupied, four unoccupied).

In particular, the HOMO-LUMO levels correspond to localized surface states that are due to the dangling bonds appearing at the (010) surfaces of the finite ribbon, where the Bi-S bonds are cut. There are two ways of passivating the

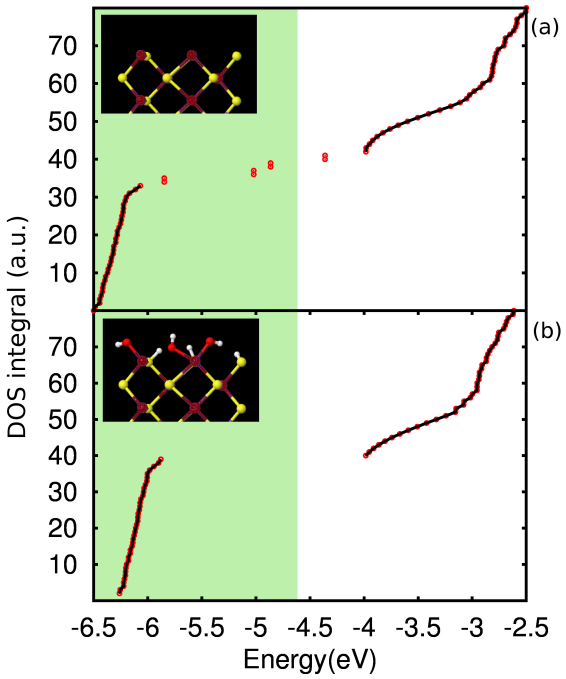

Figure 4.2: Density of states integral as a function of energy for a 10 nm-long ribbon in its experimental geometry. The green background indicates the filled molecular orbitals. (a) Before saturation. The presence of dangling bonds on the surface causes the formations of trap states in between the valence and the conduction band. (b) After saturation. H atoms and OH groups passivate the surface (see inset) and a clean HOMO-LUMO gap is obtained.

surface states: by performing structural relaxation of the system through self-healing (161, 162) or by suitable saturation of the dangling bonds. Both methods were investigated.

4.2.1 Relaxed nanoribbons

Fig. 4.4(a) reports the HOMO-LUMO gap of the Bi_2S_3 nanoribbons after atomic relaxation as a function of their length. The zero of the energy scale is set to the band gap of the relaxed infinite ribbon. Let us examine first the part of the curve associated with ribbons longer than 2 nm. The inverse dependence of the HOMO-LUMO gap from the size (*quantum confinement*) is very little:

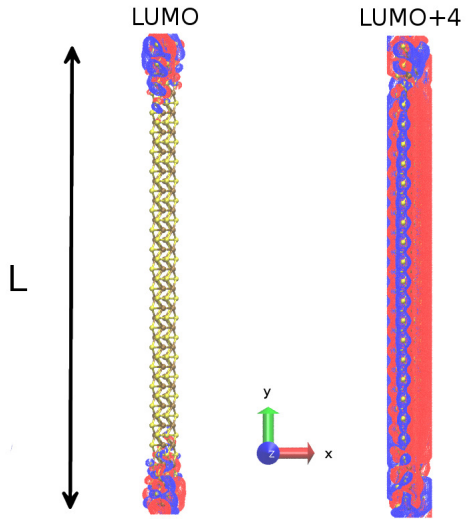

Figure 4.3: A direct space representation of the molecular orbital isosurfaces. (a) The Lowest Unoccupied Molecular Orbital (LUMO). The orbital is confined to the ribbon edges: in fact, it is a surface state due to the presence of dangling bonds. (b) The LUMO+4. The orbital is fully delocalized and belongs to the conduction band.

the gap converges fast to the asymptotic value with a power law $\propto L^{-2}$ and variations of tens of meV when the length is increased by 1 nm. A more unusual feature is observed when relaxing ribbons shorter than 2 nm where an abrupt lowering of the gap by about 1 eV (from 1.6 to 0.7) eV is observed. In order to validate the above behavior the atomistic relaxations were repeated with the B3LYP exchange-correlation functional. Although the B3LYP overestimates the absolute value of the band gap with respect to PBE, it provides the same band gap dependence on size and it validates the occurrence of the same jump below 2 nm. In addition, since recent computational results show that the DFT Kohn-Sham gap is sensitive to the inclusion of Bi semi-core shell, spin-orbit coupling, and quasi-particle gap correction (145), we took explicitely into account all of the above effects to check the validity of the methodology adopted. Fig. 4.5 compares the PBE Kohn-Sham gap dependence on size with and without spin-orbit and quasi-particle effects. In the calculation with the spin-orbit correction (163), the Bi $5s^2\ 5p^6\ 5d^{10}$ semi-core shell (164) has been included. The quasi-particle gap has

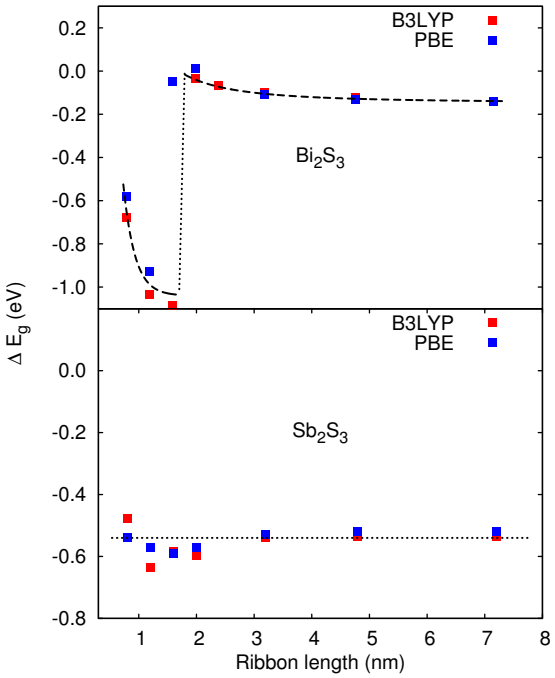

Figure 4.4: DFT Kohn-Sham gap variation as a function of the ribbon length after relaxation. The zero of the energy scale is set to the PBE band gap of the relaxed infinite ribbon (1.53 eV and 1.62 eV for Bi_2S_3 and Sb_2S_3, respectively); the B3LYP and PBE asymptotes have been aligned. (a) Bismuth sulfide. An abrupt transition is observed at 2 nm. For long ribbons, the HOMO-LUMO gap converges to the value of the periodic case (b) Antimony sulfide. No transition is observed. The ribbons are unable to self-repair their defects and the HOMO-LUMO gap does not converge to the value of the periodic ribbon.

been evaluated through the ΔSCF method as difference between the ionization energy and the electron affinity of each cluster (140). As shown in the figure, the explicit inclusion of all the above effects does not change importantly the functional gap dependence on size. In particular, it is still found a jump and a $\sim L^{-2}$ decay. From a quantitative point of view the combined effect of spin-orbit and semi-core is to lower by about ∼0.2 eV only the long ribbons energy gap. Conversely, the band gap of small ribbons are unaffected. In practice, the spin-orbit correction is always about −0.2 eV while the semi-core correction is +0.2 eV for small ribbons and almost zero for long ribbons. A small reduction of the gap

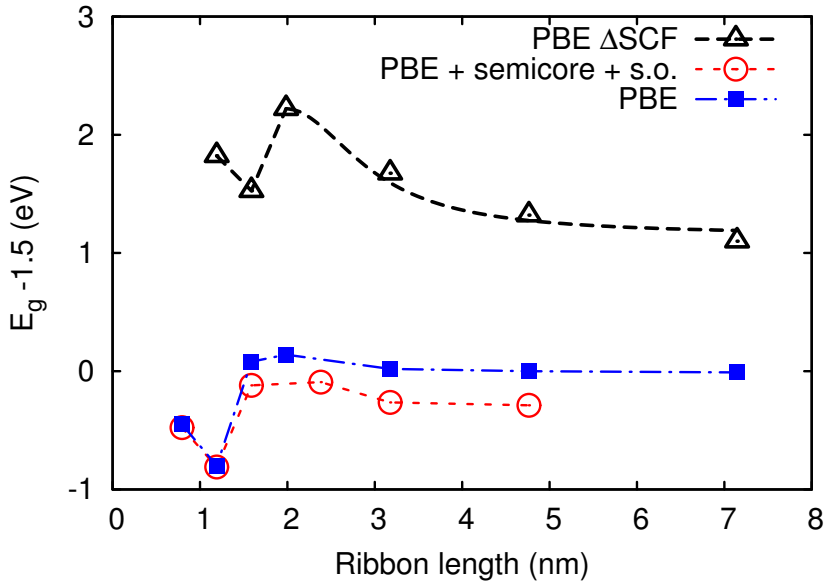

Figure 4.5: Calculated gap dependence on size according to different corrections to PBE: no corrections (blue); spin-orbit and Bi semi-core states (red); quasi-particle correction through the ΔSCF method (black). The lines are guides to the eye. The zero of energy is set to 1.5 eV, i.e. the asymptotic value of PBE blue curve.

discontinuity is therefore calculated by including spin-orbit coupling and semi-core electrons with respect to DFT. As for the quasi-particle effects, consistently with the GW result for the bulk material (145), the ΔSCF gap calculated for finite ribbons is larger than the corresponding DFT gap. However, for finite ribbons, the difference between quasi-particle and DFT gap is considerably larger due to the sizable exciton binding energy expected for finite systems. Overall, there is no significant difference as far as the HOMO-LUMO gap dependence on size is concerned. The entire discussion on quantum confinement is therefore not affected significantly by the explicit inclusion of spin-orbit, semi-core, and quasi-particle effects. Figure 4.6 shows separately the variation of the B3LYP HOMO and LUMO energies as a function of the size. The jump of the HOMO-LUMO gap at ∼2 nm is associated to two corresponding steps in the two curves. The two insets in Fig. 4.6 show the HOMO spatial distribution of a 4-units ribbon (left) or 5-units ribbon (right) around the length of the discontinuity in the electronic gap.

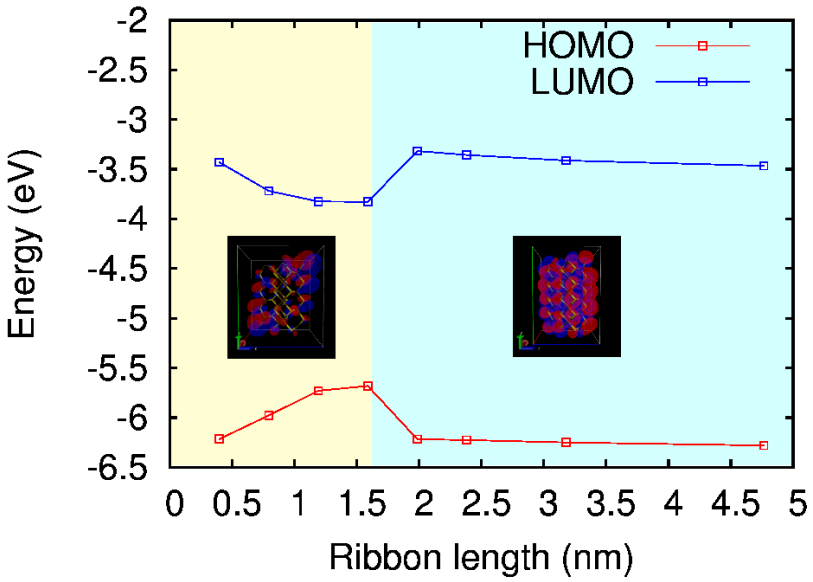

Figure 4.6: B3LYP HOMO and LUMO energy as a function of the ribbon length. For ribbons shorter then 2 nm both the MO are localized surface states (left inset). For ribbons longer of 2 nm, relaxation passivates the surfaces and fully delocalized HOMO and LUMO are observed (right inset).

The HOMO level of nanoribbons shorter than 2 nm is localized on the edges (left inset). Only for ribbons longer than 2 nm the HOMO is delocalized on the whole crystal structure (right inset). One concludes that the ribbons shorter than ∼2 nm are unable to get rid of their surface states by means of atomic relaxation and still contain localized levels inside the gap. Only for ribbons longer than 2 nm a complete reconstruction of the surfaces is possible providing the disappearance of defect states and restoring a clean gap. It is interesting to compare these observations with a different pnictogen sulfide having the same crystal structure. To this aim atomic relaxations on stibnite ribbons were performed. As shown in Fig. 4.4(b) the HOMO-LUMO gap is practically independent on size with no large discontinuities. The asymptotic value of finite nanocrystals is 0.4 eV lower than that of periodic ribbons. This demonstrate that Sb_2S_3 is unable to completely self-repair its dangling bonds by surface reconstruction even in the case of 10 nm long ribbons and the remaining surface states within the gap hinder the occurrence of a clear trend in the HOMO-LUMO gap dependence on size. In order

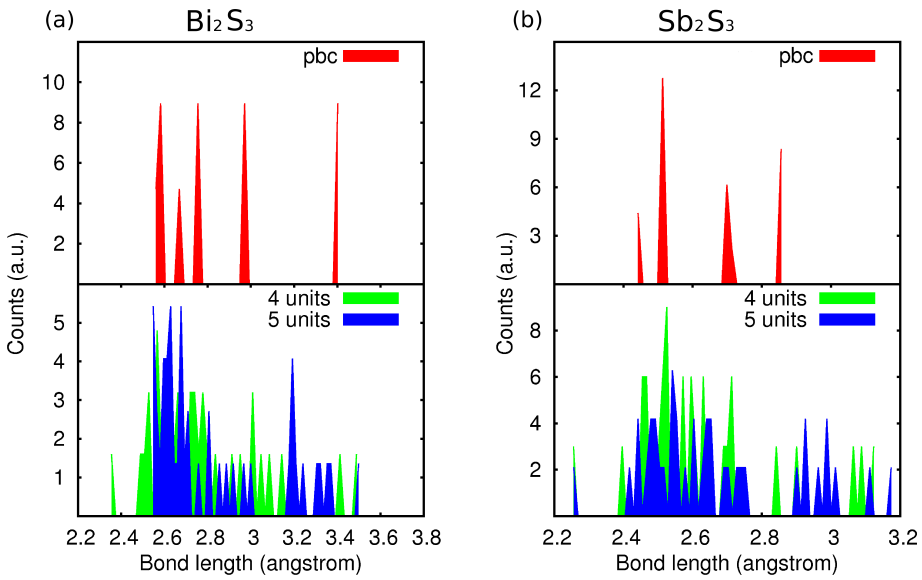

Figure 4.7: Bond length distribution of standalone ribbons after relaxation. (a) Top: bond distribution for the periodic Bi_2S_3 ribbon. Bottom: bond distribution for ribbons shorter (green) and longer (blue) than the HOMO-LUMO gap transition length. The formation of new bonds for long ribbons causes a redistribution of the atomic distances and the disappearance of the short bonds. (b) Bond distribution of Sb_2S_3. In this case, there is no formation of new bonds and the bond distributions of the two finite ribbons are qualitatively similar.

to correlate the above gap dependence on size to morphological features, the bond length changes upon relaxations of nanoribbons of different length were studied. In particular, the bismuth-sulfur distance for all atom pairs within the ribbon was calculated and the corresponding number distribution (number of bonds as a function of their length) reported in Fig. 4.7. In that figure, panel (a) reports a comparison between the Bi-S bond distribution in the relaxed periodic ribbon (red), the ribbon of length 4 unit cells (green) and 5 unit cells (blue). These latter systems delimit the discontinuity in the bangap-to-length curve (see Fig. 4.4 and Fig. 4.6). It is clear that the two finite ribbons differ strongly in their Bi-S bond distribution despite their very similar length. Two major differences can be identified. Going from five to four unit cells, a significant disorder is induced as shown in the larger distribution of lengths found for the 4 units system. Secondly, a short bond of 2.4 Å is created, which is not present in the ribbons longer than

4 units. Such variations of the ribbon morphology occur only when passing from 4 to 5 units ribbons. The short bond formed for ribbon lengths < 2 nm is related to a shortening of the Bi-S bonds involving undercoordinated S atoms at the surfaces. By inspecting the geometrical relaxation of systems of different

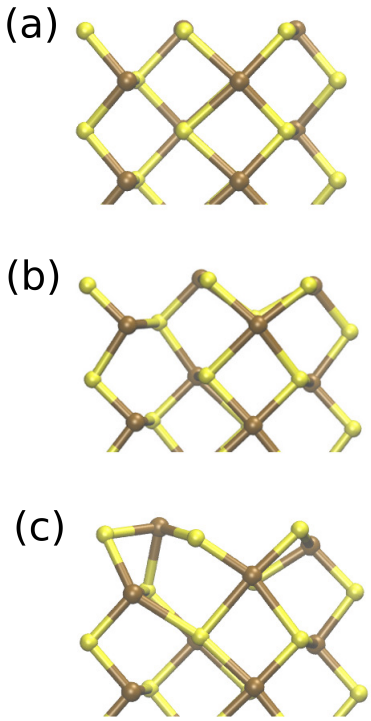

Figure 4.8: (a) Unrelaxed ribbon (experimental geometry). (b) Relaxation of a ribbon shorter than 2 nm. No new bonds are formed. (c) Relaxation of a ribbon longer than 2 nm. The atoms at the surface recombine to passivate dangling bonds.

length it can be seen that the ribbons longer than 2 nm undergo a particular reconstruction at the surfaces that involves the saturation of the dangling bonds through the formation of new bonds (Fig. 4.8). Such a reconstruction is not energetically convenient for ribbons shorter than 2 nm. In this case the sulfur atoms at the surface are not able to form new bonds and their Bi-S bond length is substantially decreased preventing electron sharing with other surface atoms. The results for Bi_2S_3 are quite different from the case of Sb_2S_3 ribbons. In Sb_2S_3

relaxed ribbons there is no surface reconstruction for any size investigated (up to 10 nm) (see Fig. 4.7(b)) and there is always a short bond of about 2.3 Å in the bond distribution.

The ribbon relaxation was further characterized by calculating the squared effective length $\lambda^2 = \sum_i y_i^2$ along the [010] direction and the relative variation $\Delta y = \sqrt{\frac{\lambda^2 - \lambda_0^2}{\lambda_0^2}}$ with respect to the square length of the same nanocrystal at equilibrium (λ_0). The results are reported in Fig. 4.9. For both Bi_2S_3 and Sb_2S_3,

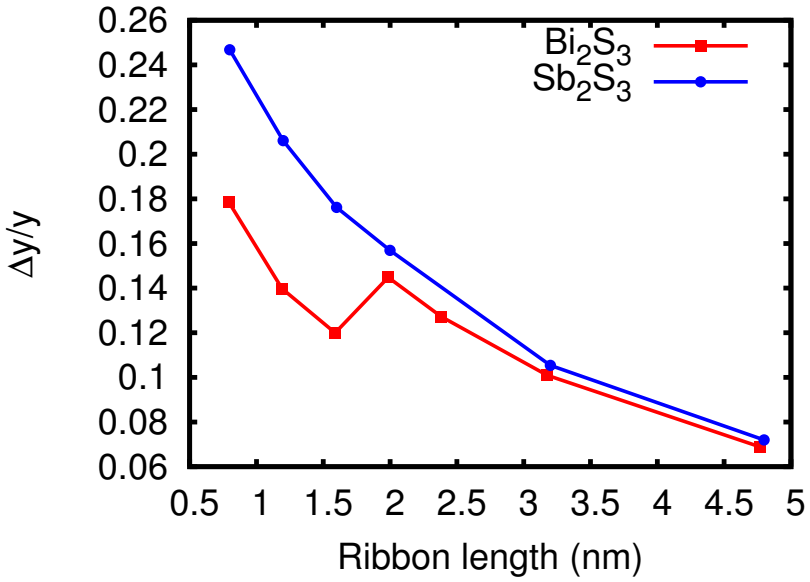

Figure 4.9: Relative elongation of the ribbons as a function of their length. Sb_2S_3 shows a smooth trend, where the elongation monotonically decreases with increasing length. On the other hand, Bi_2S_3 presents a step occurring exactly at the HOMO-LUMO gap transition length.

there is a relative y-elongation (tensile strain) of the finite length ribbon with respect to the infinite one. The tensile strain increases for shorter ribbons as expected from the fact that the excess energy density $u = E_S/V$ due to the surfaces is proportional to the surface-to-volume ratio S/V. In fact $u = E_S/V = 2\gamma S/V \sim \frac{2\gamma}{L}$, where γ is the surface energy of the (010)-plane and L is the ribbon length. Consistently with the fact that Sb_2S_3 nanocyrstals do not exhibit a change in surface reconstructions, the elongation turns out to be a monotonically decreasing function of the ribbon length. At variance, in the case of Bi_2S_3, a step

was found at 2 nm in the strain function that corresponds to the different surface reconstructions discussed above.

Overall the above analysis shows that the fine interplay between the strain and surface reconstruction induce a non-monotonic dependence of the HOMO-LUMO gap of the relaxed Bi_2S_3 ribbons. This makes difficult to recognize the occurrence of quantum confinement. In order to disentangle the role of atomic relaxations and surface effects from quantum confinement an additional analysis was performed by accurately saturating unrelaxed nanostructures.

4.2.2 Saturated nanocrystals

A second set of Bi_2S_3 nanoribbons (hereafter referred to as unrelaxed) is obtained by removing the surface states by chemical saturation of the dangling bonds while keeping ribbons in their perfect crystal geometry at experimental lattice size. The undercoordinated sulfur and bismuth atoms on the ribbon edges are saturated by H and OH groups, respectively (see inset in Fig. 4.2(b)). A local relaxation is performed where only saturating atoms are allowed to move. The resulting electronic structure gives a clean HOMO-LUMO gap with no surface states occurring in the ribbons (Fig. 4.2(b)). The change of the gap as a function of the ribbon length (ΔE_g) is reported in Fig. 4.10(a), in which both the PBE and B3LYP results are present. The zero of the energy scale corresponds to the unrelaxed infinite ribbon gap. As one can see, there is a monotonic increase of the HOMO-LUMO gap with decreasing size consistent with a sizable quantum confinement of electrons in the system. This behavior can be nicely reproduced by a power law function of the ribbon length $f(L) \propto \frac{1}{L^2}$. It is important to note that L^{-2} is the standard quantum confinement law. Fig. 4.10(a) reveals that it is possible to significantly tune the HOMO-LUMO gap only for nanocrystals smaller than ~ 3 nm: for larger systems quantum confinement is hardly detectable. For long unrelaxed Bi_2S_3 ribbons, the gap converges to the value of the infinite ribbon. It should be noticed that the overall electronic confinement attainable by reducing the ribbon length is around 0.6 eV for both PBE and B3LYP, much higher than the quantum effect observed when passing from the bulk to the infinite ribbon (0.1-0.2 eV). That means that the electronic coupling between neighbor ribbons

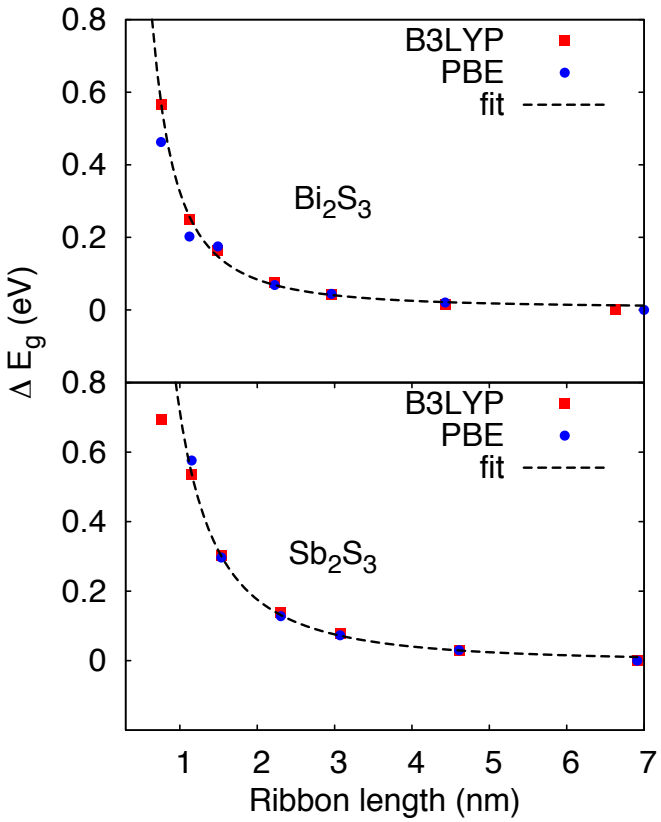

Figure 4.10: Quantum confinement energies of saturated ribbons as a function of their length calculated by PBE (circles) and B3LYP (squares) functionals for Bi_2S_3 (top panel) and Sb_2S_3 (bottom panel). Dashed lines correspond to numerical fit (see text).

plays only a secondary role in the delocalization of the electrons: the confinement is primarily due to the length of the ribbons.

The above analysis has been repeated for the case of Sb_2S_3 unrelaxed ribbons as well. The results are reported in Fig. 4.10(b) and the HOMO-LUMO gap has the same L^{-2} asymptotic behavior of Bi_2S_3 case. In both cases, sizable variation of the gap are expected only for nanostructures smaller than about 3 nm.

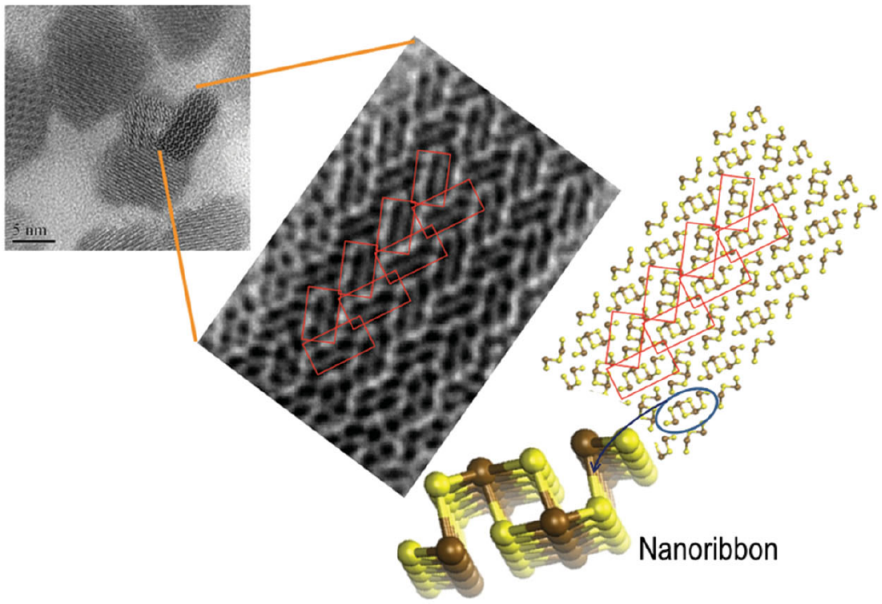

Figure 4.11: High-resolution transmission electron microscopy (HRTEM) image of the synthesized Bi_2S_3 nanocrystals. By comparison with the ball-and-stick model of Bi_2S_3, one can recognizes the herringbone pattern of nanoribbons extending along the [010] crystallographic direction.

4.2.3 Comparison with the experimental results

In this section, a comparison between the theoretical predictions and the experimental data is given. The reference work (19) concerns three samples of Bi_2S_3 nanoparticles obtained through colloidal synthesis. The size of the nanoparticles ranges from 3.6 nm to 29 nm, depending on the sample considered (see more details in section 4.4). According to spectroscopic data, the room temperature absorption spectrum near the optical gap is dominated by band-to-band transitions and a broad excitonic contribution.(165) The band gap energy, E_g, was found to be at 1.443 eV and the exciton transition at 1.413 eV. To investigate the effect of the nanocrystal size on the lowest energy electronic levels in more detail, Fig. 4.12(a) reports a zoom near the edge of the absorption spectra together with their first derivatives; these latter can reveal weak optical contributions and minute differences in the spectra with enhanced sensitivity. The derivative spec-

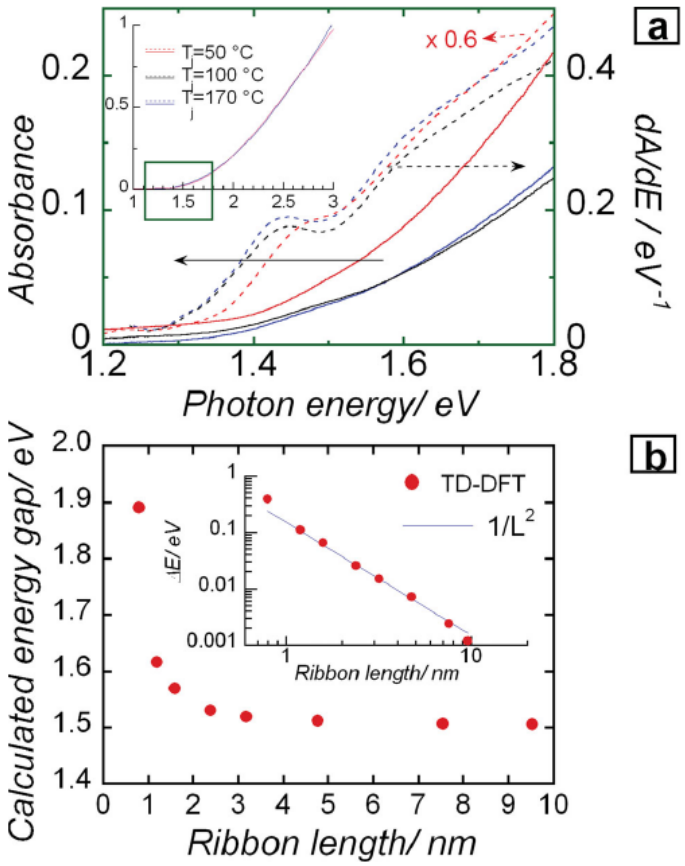

Figure 4.12: (a) Absorbance spectrum (continuous lines) and its first derivative (dashed lines) near the absorption edge of Bi_2S_3 nanocrystals in toluene dispersion synthesized at the injection temperatures, T_j = 50, 100, and 170 °C, respectively (see details in Sec. 4.4). The inset shows the whole UV-Vis-NIR spectra. For sake of comparison, spectra for T_j = 50, 100 °C are rescaled to the intensity of the spectrum for T_j = 170 °C. (b) Theoretical energy gap and energy gap shift (inset) of a single ribbon as a function of the ribbon length L. The lowest excitation energy was calculated through first principles methods in the framework of the time-dependent density functional formalism.

trum shows that in the sample containing the smallest nanocrystals the shoulder is blue shifted by 30 meV. These spectroscopic data demonstrate that the quantum size effect is detectable but limited, despite the small dimension of the Bi_2S_3 nanocrystals. It is also worth comparing the observed shift with the confinement energies observed in nanocrystals with well-studied optical properties, such as

CdSe, CdS or PbS, and PbSe. For a particle size of ∼3.5 nm, the increase of the optical gap is several hundreds of meV, at least an order of magnitude higher than in Bi_2S_3.(166, 167, 168, 169)

To take into account the excitonic contribution to the band gap, the previous atomistic calculations on the saturated single ribbons were repeated within the time-dependent density functional theory (TDDFT, see Chapter 2). The calculated excitonic optical gap of the ribbon is reported in Fig. 4.12(b) as a function of the nanoribbon length L. The band edge saturates at 1.5 eV for long chains. The optical gap dependence on size follows a $1/L^2$ behavior. Theoretical data show that the gap tuning becomes perceptible only for ribbon length L around 3 nm. Blue shifts larger than one hundred of meV is achieved when L is smaller than 1 nm.

A few comments are required in order to compare the experimental and theoretical values of the band gap tuning in Bi_2S_3. It is important to observe that the lengths of the nanoribbons forming a spherical nanocrystal of diameter D are distributed in the range $0 < L < D$: the ribbon passing through the center of the nanoparticle has a maximal length $L = D$ while peripheral ribbons must be shorter. In other words, assuming an ensemble of spherical nanocrystals, all with the same diameter D, there exists an intrinsic distribution of ribbon lengths, as shown in Fig. 4.13. Here, a simple algebrical relation between the average ribbon length and particle dimension in ideal spherical nanocrystals is provided. Let consider a sphere of diameter $D = 2R$ (see 4.14) formed by a bunch of N ribbons oriented along z-direction (*Pbnm* notation) having a constant density $\sigma = N/(\pi\rho^2)$ in the xy-plane. The height of ribbons located at a distance ρ from the z axis is:

$$h(\rho) = 2\sqrt{R^2 - \rho^2} \tag{4.1}$$

The fraction of ribbons located at a distance ρ within the element of area $dS(\rho)$ is

$$df(\rho) = \frac{\sigma dS(\rho)}{\sigma \pi R^2} = \frac{2\pi\rho d\rho}{\pi R^2} \tag{4.2}$$

The average height $< L >_D$ of ribbons forming the sphere depends on its diameter

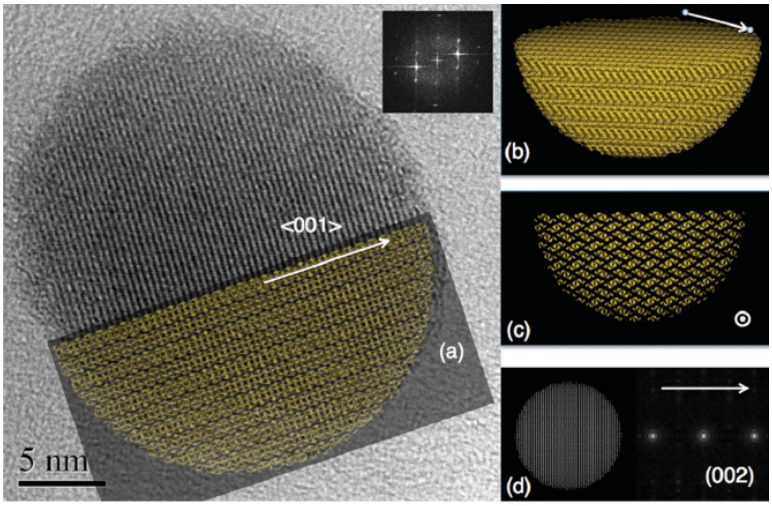

Figure 4.13: a) HRTEM image of a spherical nanocrystal with the superimposed ideal crystalline structure formed by ribbons aligned along the <001> direction (*Pbnm* notation here considered); FFT (fast Fourier transform) of the HRTEM image in the top right corner. Perspective view (b) and cross section (c) of the atomistic crystalline structure showing the herringbone motif formed by the nanoribbons. (d) Calculated FFT (right side) of the crystal image (left side) revealing the (002) inter-plane spacing corresponding to the experimental inter-plane distance of 0.39 nm.

D and it can be calculated as

$$< L >_D = \int_0^R df(\rho)h(\rho) = \int_0^R \frac{2\pi\rho}{\pi R^2} d\rho \, 2\sqrt{R^2 - \rho^2} \tag{4.3}$$

from which it is found that

$$< L >_D = \frac{2}{3} D \tag{4.4}$$

At the peak of the particle size distribution (3.5 nm), the average ribbon length is thus expected to be 2.3 nm. The expected shift of the absorption edge is calculated numerically in the continuum model from the knowledge of the dependence of the theoretical band gap shift on L. It is assumed that the lowest excitonic absorption is given by the sum of the absorption line from each nanoribbon in a spherical nanocrystal of radius $R = D/2$. The resulting absorption spectrum

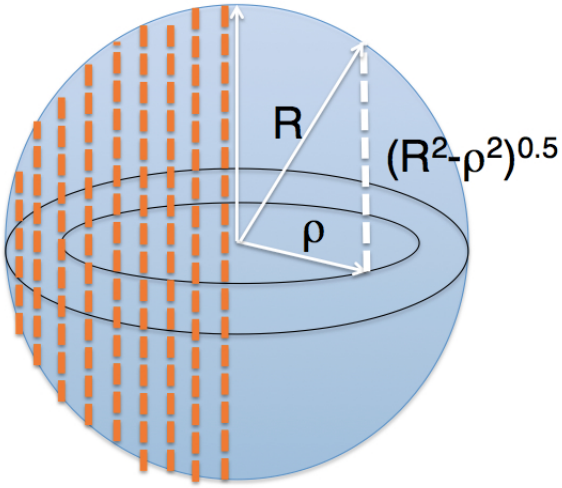

Figure 4.14: Schematic representation of a spherical nanoparticle formed by ribbons of different lengths (dashed lines) in the continuum approximation.

reads:

$$< E >= \int_0^R g[E - E_i(\rho)]\sigma(\rho)df(\rho) \tag{4.5}$$

where $E_i(\rho)$ and $\sigma(\rho)$ are, respectively, the exciton transition energy and absorption cross-section in the ribbon placed at a distance ρ from the center of the nanocrystal reported in Fig. 4.14; $E_i(\rho)$ and $\sigma(\rho)$ are calculated through first-principle time-dependent density functional theory; df(ρ) is the fraction of ribbons located at a distance ρ within the element of area dS(ρ). A gaussian shape $g(E)$ of width Δ is taken for the excitonic absorption line. Δ ~100 meV is assessed from the first derivative of the absorption spectrum shown in Fig.4.12, specifically, from the energy spacing between the maximum and minimum of the S-shaped derivative spectrum near the excitonic transition. The calculated absorption spectra and their first derivatives are shown in Fig.4.15 for $D = 3.5$ nm and $D = 14.7$ nm. For $D = 3.5$ nm, a ~30 meV blueshift of the absorption peak is found, while for the larger nanocrystal the confinement effect is negligible. In this size range, the calculated optical shift corresponds in good approximation with the blueshift calculated for a nanoribbon of length $< L >_D$. In this size range, the calculated optical shift corresponds in good approximation with that calcu-

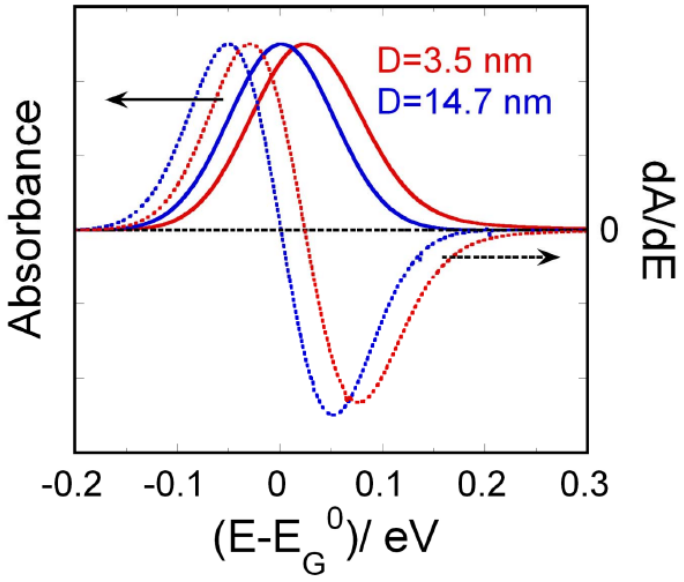

Figure 4.15: Absorbance and its first derivative near the lowest excitonic transition in spherical nanocrystals calculated within the continuum model. For sake of comparison, spectra are normalized to their maximum. E_G^0 is the optical gap energy of bulk Bi_2S_3.

lated for a nanoribbon of length $< L >_D$. We find a blueshift of 30 meV, in good agreement with experiments. The possibility to achieve the challenging regime of strong confinement ($< L >_D$ ~1 nm, D ~1.5 nm) with useful energy shifts of several hundreds of meV is not, however, out of reach. According to previous experimental reports, nanocrystals with size around 1.6 nm can be effectively synthesized by using a different synthesis approach; the observed experimental band gap shift is consistent with the present theoretical model.(57)

A short discussion on the origin of the smaller Bi_2S_3 band gap shift with respect to other semiconductor nanocrystals (such as Cd and Pb chalcopyrites) is necessary. According to basic concepts of quantum mechanics, the energy shift of the lowest confined level in an infinite potential well is expected to scale with the well size (D) and the effective mass (m_{eff}) of the excitation, following the equation

$$\Delta E = \frac{Ch^2}{8m_{eff}D^2} \tag{4.6}$$

where h is the Planck constant while and C is a constant that depends on the dimensionality of the confining potential. For a 1D-potential, suitable for Bi_2S_3 ribbons, $C = 1$, while for a 3D-spherical well, which describes the case of most nanocrystals made by II-VI and III-V semiconductors, $C = 4$.(170, 171) This larger value accounts for the confinement energies along the three spatial dimensions ($C = 3$ corresponds to the case of a particle in a 3D-square well). This analysis suggests two main reasons for the comparatively small band gap shift observed in Bi_2S_3 nanocrystals: (i) the 1D-character of the band-edge electronic states, and (ii) their heavy mass.(122, 145)

4.3 Nanowires

This section is dedicated to the study of ultrathin nanowires (NWs) obtained by the aggregation of more than one nanoribbon. The stability of NWs formed by 4, 7, and 9 nanoribbons is investigated by means of both theoretical and experimental methods. Their surface states, passivation and defects are further investigated within the framework of DFT providing a possible route for improving the opto-electronic properties of Bi_2S_3 elongated nanostructures.

4.3.1 Energetics of the nanowires

The thermodynamic stability of nanoparticles is determined by their total configurational energy; the most stable atomic configurations are those with the lowest energy values. For thin nanowires formed by a small number of ribbons it is possible to calculate their energy from first-principles. We consider NWs of increasing diameter built of 1, 4, 7, 9 ribbons, respectively (see Fig. 4.16). In particular the largest 9-ribbons model has a diameter as large as 3 nm. All the NWs are periodic along the ribbon axis and are obtained by cutting the corresponding number of ribbons from a perfect bulk followed by the full relaxation of atomic structure through conjugate-gradient minimization.

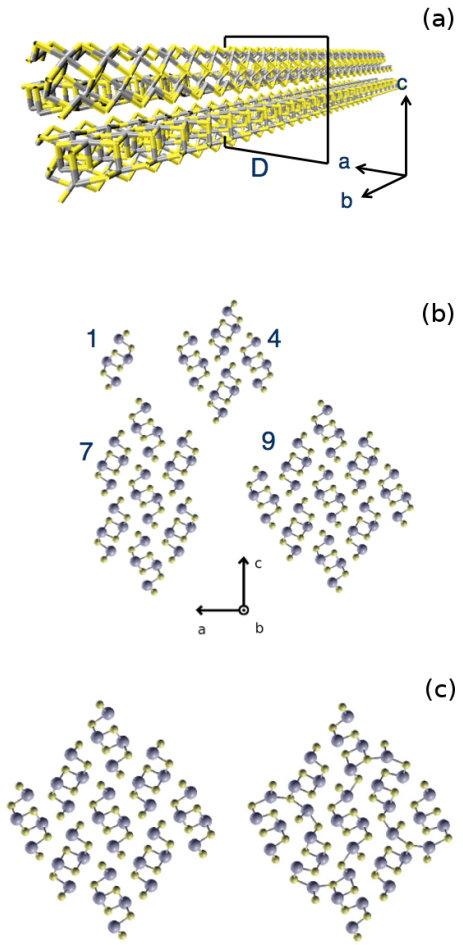

Figure 4.16: Panel a: Perspective view of an atomistic model of Bi_2S_3 NW extending along the b direction; Panel b: Cross section view of NWs composed by one, four, seven, and nine ribbons. Panel c: Comparison between a NW before (left) and after (right) energy minimization.

The cohesive energy per atom, ΔE, of the nanowires is defined as

$$\Delta E = \frac{E - r \cdot E_{rib}}{N} \tag{4.7}$$

where E is the total energy of the NW formed by r ribbons and N atoms and E_{rib} is the total energy of the single isolated ribbon. A negative value of ΔE means that the wire is stable against its separation into isolated ribbons. The lower is ΔE the higher is the stability and the cohesion between ribbons.

The results for ΔE are reported in Fig. 4.17. The cohesive energy of the

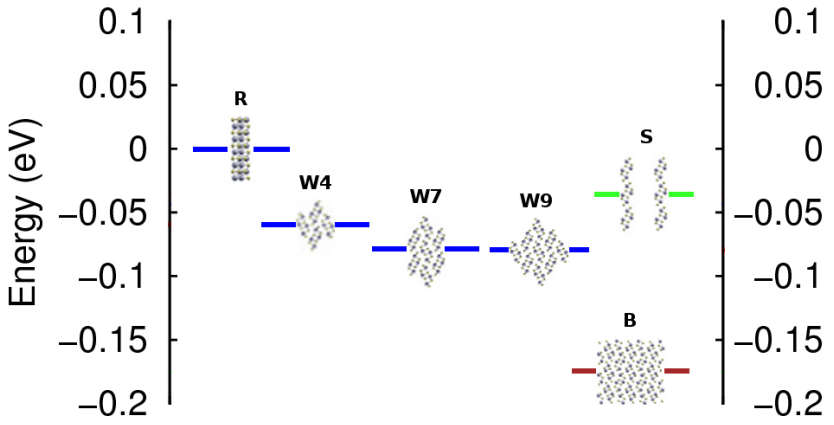

Figure 4.17: Energy difference per atom, ΔE, of the Bi_2S_3 nanostructures. The nanowires (W4,W7,W9) get more stable with respect to the single ribbon (R) by increasing their diameter. Also the cases of a lamellar structure along the z-direction (S) and the bulk (B) are reported for comparison.

single ribbon is zero by definition. At larger diameters of the NWs, ΔE decreases monotonically i.e. the structures become more stable. The bulk is found at $\Delta E = -0.18$ eV/atom and it represents the lowest value attainable in the limit of NWs with infinite diameters. We also considered for comparison the case of ultrathin Bi_2S_3 lamellar structures (Fig. 4.17, S) formed by a regular array of parallel ribbons. In particular we calculated the energy of the z-oriented lamellar structure that provides the preferential inter-ribbon electronic coupling and the largest energetic stability. The calculated energy suggests that, though possible, lamellae are higher in energy than cylindrical NWs. We expect that the former will spontaneously fold into NWs by an exothermic relaxation.

Overall, the above analysis shows that the NWs formed by seven or more ribbons have an energy gain of about 80 meV/atom with respect to the single ribbon. This is large enough to compensate the thermal energy at room temperature, so allowing the formation of stable structures of assembled ribbons. By

comparing the energy of the NWs with respect to the bulk we can estimate a moderate excess energy associated to the large surface-to-volume ratio of about 0.1 eV/atom. Though higher in energy than the bulk, the NWs do not undergo phase transformations or amorphization during the relaxation of atomic forces. During the relaxation of the NWs (see Fig. 4.16, panel c) the sulfur atoms of the surfaces tend to move inwards in order to compensate for the reduced atomic coordination with respect to the bulk, generating a strain on the surfaces. Apart from the above strain effects, the NWs preserve their overall crystallinity.

4.3.2 Synthesis

The theoretical results show that crystalline Bi_2S_3 ultrathin NWs grown along the [010] crystallographic direction are in principle stable. This result is consistent with experiments, as we are able to synthesize crystalline nanostructures with comparable diameters by performing an oleylamine based organometallic synthesis (see Section 4.4). Fig. 4.18 (left) reports the transmission electron mi-

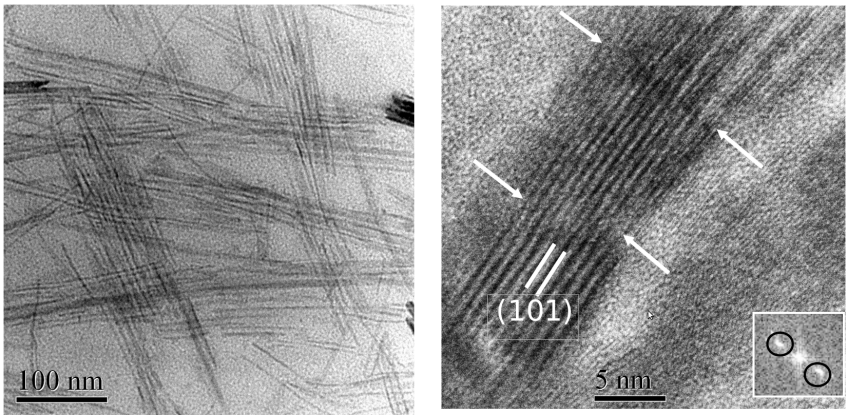

Figure 4.18: Left: TEM image of Bi_2S_3 nanowires, obtained by oleylamine-based colloidal synthesis. Right: HR-TEM image of a portion of Bi_2S_3 nanowire, where nanocrystals are iso-oriented along the [010] direction; grain boundaries are present between the nanocrystals (arrows)

croscopy (TEM) image of Bi_2S_3-NW samples. The colloidal dispersion in toluene was very stable. NWs with an average width of 3-4 nm and lenghts exceeding 300 nm were obtained. X-ray diffraction pattern indicates the presence of or-

thorhombic bismuthinite as a single crystalline phase. The high resolution TEM (HR-TEM) shows that the coherence length of the NWs is around 30 nm (see Fig. 4.18)(right). It also highlights that the (101) planes are perpendicular to the NWs axis, i.e. the wires grow along the [010]-direction. Imperfections similar to grain boundaries can be attributed to the growth mechanism of the NWs, which consists in the consecutive nucleation of nanocrystals on the elongated structure. However, each nanocrystal preserves the crystallographic orientation of the wire. The boundaries can be better explained as small variarion of the NW diameter, while the core crystalline structure is common to all the nanocrystals. The preferential orientation of the NWs makes them linear, at variance with the case of Bi_2S_3 ultrathin NWs reported so far in literature, that are flexible and do not exhibit a long-range crystallographic order.

4.3.3 Electronic properties of the nanowires

In Fig. 4.19 we report the electronic density of state (DOS) of the crystalline bulk (Panel a) and of the 4-ribbons NW (Panel b). Occupied states are represented by filled curves. We identify two main features of the nanowire DOS that are not present in the bulk: (1) a peak at 300 meV above the valence band corresponding to the highest occupied level of the NW; (2) an increase of the density of states close to the top of the valence band. The two features are observed in all the NWs investigated. We discuss first the point (1). By analyzing the atomic projections of the electronic wavefunction it is found that the highest occupied states are p-type orbitals localized on the outer edge sulfurs of the NWs (see the magenta lobes in Fig. 4.19, right). Interestingly, the density of the surface states involves mainly two lines of sulfur atoms at the opposite edges of the NWs instead of being distributed over all external sulfur atoms. These states are doubly degenerate since there are two sulfur atoms within each unit cell that are equivalent by simmetry.

In order to better characterize the nature of the states we analyze the band structure of the NW (See Fig. 4.20, panel a). It is found that, along the $\Gamma - Y$ direction, the two degenerate defect lines located above the continuum valence band are not flat but are rather dispersed in energy following the shape of the

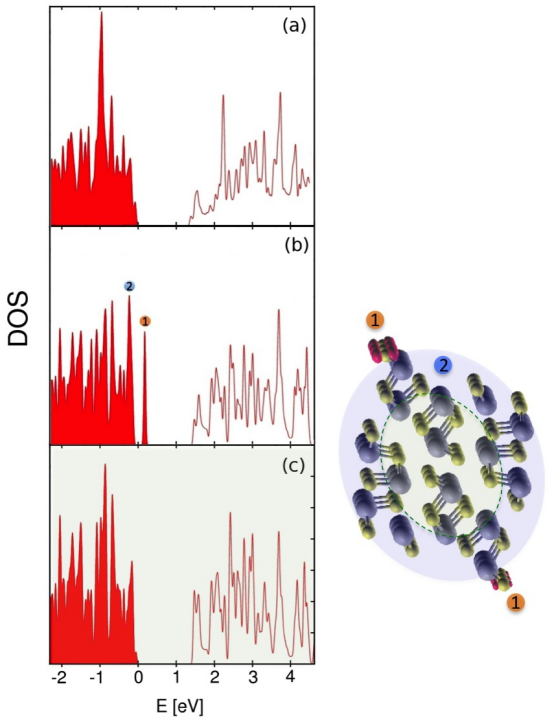

Figure 4.19: Left: DOS of the Bi_2S_3 bulk (a) and the 4-ribbon nanowire (b); Panel c reports the nanowire DOS projected on its core atoms (see text). Right: Representation of the core (green) and surface (blue) of the NW; the valence top orbital localized on the sulfurs atoms at the nanowire edges are also shown (magenta color).

valence band. We conclude that the defect states are delocalized along the ribbon (y-direction). The above analysis shows that the peak 1 can be attributed to the edges of the ribbon that induce electronic states localized within the plane perpendicular to the ribbon (x-z plane) but delocalized along the ribbon y direction. We conclude that the peculiar crystalline structure of Bi_2S_3 NWs formed by weakly interacting ribbons results in 1D-like surface states at the NWs edges. Interestingly, the energy position of this levels (0.3 eV above the valence band) is compatible with the results of spectroscopic measurements in Bi_2S_3(19).

The surface of the NW is also responsible for the DOS peak 2. At variance with the previous case, these levels are not localized on a specific atom and can be attributed to the strain of the surfaces (represented by the blue region in the atomistic model of Fig. 4.19, right). In order to validate this hypothesis

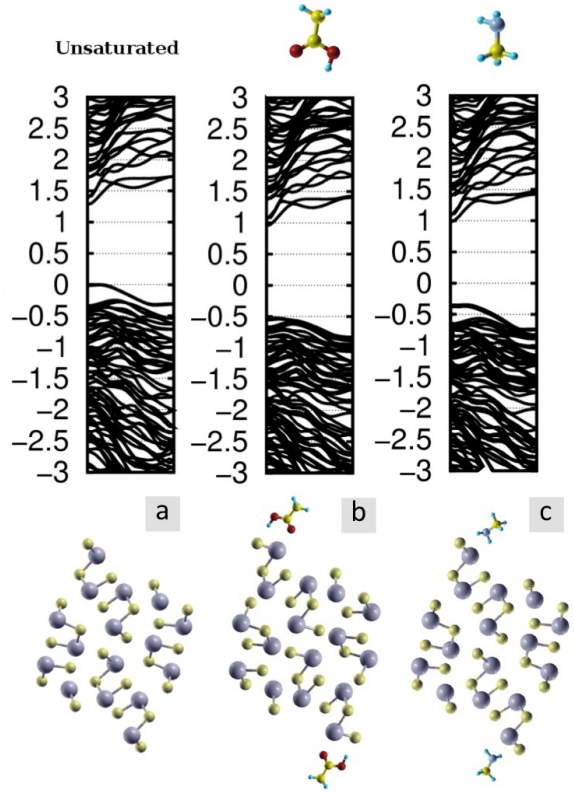

Figure 4.20: Band structure of the 4-ribbon nanowire before (left) and after saturation with acetic acid (center) and methylamine (right). Acetic acid appears to be more efficient in lowering the surface band below the valence band. Minimum energy configurations of 4-ribbons nanowire decorated by acetic acid (top) and methylamine molecule (bottom).

we calculate the core-projected DOS (Fig. 4.19, c) obtained by considering the atoms forming the core of the ribbon (green region in the atomistic model of Fig. 4.19, right). By choice, the core consists of those atoms that are separated by at least 4 Å from the surfaces. Upon core-projection, not only the peak 1 disappears but we found a sizable decrease of the DOS at the top of the valence band (peak 2), so that the projected DOS is more similar (though not identical) to the bulk. This trend is further confirmed by larger ribbons for which the fraction of atoms of the core is higher. It is demonstrated in this way that feature 2 is associated

to the outer region of the NWs.

4.3.4 Passivation of the nanowires by organic ligands

It is important to identify effective ways to get rid of the surface states described above by a proper saturation of the missing electronic interactions. Colloidal synthesis of Bi_2S_3 typically makes use of organic ligands such as oleic acid or oleylamine(19, 57) with carboxylic (COOH) and amine (NH_2) anchoring groups, respectively. These compounds consist in a polar head that attaches to the nanocrystal surface and a long hydrophobic aliphatic chain that acts as a shell for the nanoparticle. However it is unknown whether the molecules are able to efficiently passivate the electronic defects of the ribbon surfaces and what is the maximum concentration of surface sites that can be saturated by an organic layer of molecules. We focus on acetic acid (CH_3COOH) and methylamine (CH_3NH_2) small molecules that have the same anchoring group of oleic acid or oleylamine, respectively but with the shortest possible aliphatic tail, in order to minimize the steric repulsion between molecules. We consider a full coverage of the ribbon edges by the organic molecules, i.e. one molecule per sulfur atom of the edge.

The results show that both arrays of molecules bind to the edges of the NWs (Fig. 4.20, bottom panels). In the case of the acetic acid, the hydrogen of the carboxylic group binds to the unsaturated sulfurs of the NW, while the oxygen is oriented towards the nearest bismuth. With the methylamine molecule, the nitrogen binds to the bismuth atom that is connected with the unsaturated sulfur (see Fig. 4.20). The adhesion energy of the acetic acid on the NWs is 0.7 eV per molecule. The methylamine molecule has a lower adhesion of 0.4 eV per molecule. According to the simulations, the acetic acid does not deprotonate spontaneously in the binding with Bi_2S_3 NWs. Similar calculations performed by starting from deprotonated configurations (COO-) give rise to smaller binding energies.

The ability of ligands to restore a clean gap is shown in Fig. 4.20 (top panels) where it is reported the band structure of the 4-ribbon NW before (panel a) and after the saturation with CH_3COOH (b) or CH_3NH_2 (c). It can be observed that the saturation by acetic acid lowers the surface level below the valence band so restoring a clean gap. In the case of methylamine, the lowering is less efficient

and the defect level still remains above the valence band at Γ. Hence the acetic acid seems to be more efficient than methylamine molecules in the removal of surface states from the band gap of the Bi_2S_3 NWs. However in both cases the molecules widen the gap up to 1.5 eV and 1.4 eV for acetic acid and methylamine, respectively. It is interesting to note that molecular passivation does not affect the valence bands of the NWs that is practically unchanged with respect to the free NW. This confirms that the modification of the valence bands of the NW with respect to the bulk (discussed above as feature (2) of Fig. 4.19) is not related to the electronic defects at the edges but rather to surface strain and it is not eliminated by the organic passivation.

4.3.5 Sulfur vacancies in the nanowires

Since the edge levels of the ribbons are associated to the outer sulfur atoms of the NWs it is interesting to understand the effect of the removal of such atoms. This

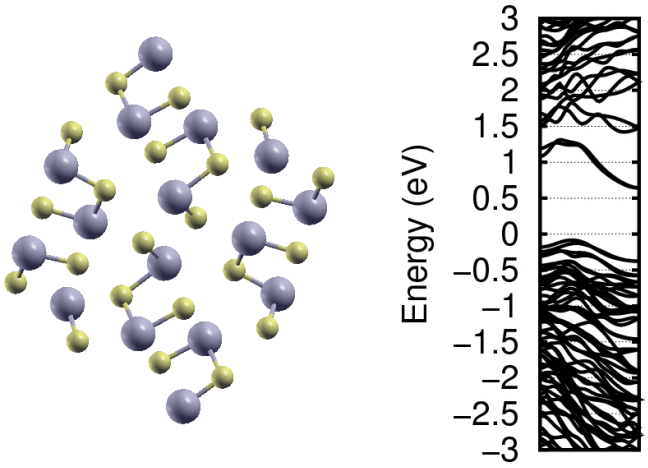

Figure 4.21: Left panel: 4-ribbon nanowire containing two sulfur vacancies (edge atoms removed). Right panel: corresponding band structure

is equivalent to consider the presence of sulfur vacancies at the NW surfaces. Actually, these kinds of point defects are known to be the most abundant in bismuth sulfide(172). We performed simulations on the 4-ribbon NW by removing sulfur atoms at the ribbon edges and fully relaxing the atomic positions. The

final NW structure is depicted in Fig. 4.21. The sulfur vacancies give rise to two doubly occupied levels deeply located within the the band gap. We conclude that sulfur vacancies are not able to compensate the surface states but generate instead doubly occupied deep states located 0.5 eV below the conduction band. Accordingly we expect to detect trap states in Bi_2S_3 samples containing sulfur vacancies, as in fact observed by spectroscopic measurements.(19)

4.4 Methodological details

4.4.1 Computational methods

Periodic structures (infinite ribbons and nanowires) were studied performing DFT calculations with the QUANTUM ESPRESSO code(129). The initial geometry was chosen corresponding to the experimental data reported by Lundegaard et al.(144) The Perdew-Burke-Ernzerhof (PBE)(132) functional within the generalized gradient approximation (GGA) was used to perform geometry optimizations. The valence electron wave functions are expanded in plane waves basis sets with kinetic energy cutoff of 30 Ry. Valence electrons are explicitly described, while the core-valence interaction is taken into account by means of Troullier-Martins pseudopotentials.(149) The reciprocal space was sampled with a (4x4x4) Brillouin zone mesh centered at Γ. Both the energy cutoff and the number of k-points were tested to be sufficient to ensure convergence of the total energy of the system. For single ribbons and nanowires the reciprocal space was sampled with a 1x4x1 mesh, according to the one-dimensionality of the systems. For the finite size nanoribbons the DFT calculations were performed with the TURBOMOLE software,(173) which is suitable for non-periodic systems. Both the PBE and B3LYP (174) functionals were employed. For the electronic wave functions the default single valence polarized (def-SV(P)) basis set of Gaussian-type orbitals in conjunction with an effective core potential including 78 (46) core electrons for Bi (Sb) was used. The accuracy of such a basis set was demonstrated by comparing the results with the computationally heavier triple-ζ valence polarized basis set (def-TZVP). To check the validity of the methodology adopted, test calculations were performed by taking into account the spin-orbit coupling (163) the inclusion

of Bi semicore states (164) and the quasi-particle correction to the DFT Kohn-Sham gaps as computed through the ΔSCF method. (140) In principle, DFT is correct only for ground-state properties of the investigated system. Optical excited states are properly described for finite systems by time-dependent DFT (TDDFT). (128) To compute the excitation energies the TDDFT implementation of TURBOMOLE was used. This latter is based on the linear response of the density-matrix, in which the poles of the linear response function correspond to vertical excitation energies and the pole strengths to the corresponding oscillator strengths. (175) The above computational methodology has been previously applied for zinc-oxide (176) and zinc-sulfide (162) nanocrystals for which a general good agreement between DFT/TDDFT results and many-body perturbation theory calculations was found. (162)

4.4.2 Experimental methods

The synthesis of the Bi_2S_3 nanocrystals was performed through an oleic acid-based organometallic synthesis. Bismuth(III) acetate, oleic acid and hexamethyldisilathiane are used as reactants and octadecene is employed as a solvent. Some parameters, such the injection temperature and the reaction time have been made to change. The mixture of 7.4100 g of bismuth(III) acetate (Aldrich >99%), 51 mL of oleic acid (Aldrich 90%) and 36 mL of 1-octadecene (Aldrich 90%) was heated under stirring in argon atmosphere at 90 °C for 16 h and then heated up to 170 °C.(94, 177, 178) A solution of 0.756 mL of HMS (Sigma Aldrich) in 30 mL of 1-octadecene was quickly injected into the fiask at the same temperature (170 °C) or after cooling down at 100 °C or at 50 °C. The kinetics of the synthesis was studied sampling at controlled times. The following acronyms will be used: $T_j = 170$, $T_j = 100$ and $T_j = 50$ °C for samples obtained at the different injection temperatures. The samples were either cooled at room temperature or quickly transferred in a beaker containing anhydrous methanol (Panreac 99.8%) soaked in an iced bath. Purification of the nanocrystals was performed by successive dispersion/reprecipitation and centrifugation steps in toluene/methanol. Finally, the nanoparticles are dispersed in anhydrous toluene (Riedel-de-Haen). These dispersions are stable for months. The reproducibility of the synthesis has

been checked and other parameters have been changed such as: the amount of the solvents and the reaction atmosphere (vacuum or argon). Neither of these parameters produced significant modification of the final product.

The nanocrystal structure and morphology were characterized by X-ray diffraction patterns were recorded on a Seifert X3000 diffractometer with a θ-θ Bragg Brentano geometry with Cu Kα wavelength. A quantitative evaluation of nanocrystal sizes through the XRD patterns was achieved by a Rietveld refinement procedure using the MAUD software:(179) recommended fitting procedure were adopted.(180) Structural model of the identified phase of Bi_2S_3 were obtained by inorganic crystal structure database ICSD [Inorganic Crystal Structure Database, ICSD, 2013 Karlsruhe, Germany]. Lattice parameters, isotropic/anisotropic average crystalline size, microstrain, preferred orientation parameter and isotropic thermal parameters were refined.(181) Weighted pattern agreement index Rw% was less than 14% for all refined patterns. Finely ground samples were dispersed in n-octane in an ultrasonic bath and the suspension dropped on a copper grid covered with a carbon thin film for the electron microscopy observation. Micrographs and selected area electron diffraction (SAED) were obtained by a transmission electron microscope (JEOL 200CX) operating at 200 kV. High resolution images were obtained by a JEM 2010-UHR equipped with a Gatan Imaging Filter (GIF) with a 15 eV window and a 794 slow scan CCD camera.

As for the transient differential transmission spectroscopy, the laser source was a Ti:Sapphire regenerative amplifier (Quantronix Integra C) operating at a repetition rate of 1 kHz and emitting at 786 nm in wavelength. The white-light continuum 150 fs-long laser pulses, generated by focusing the output of the regenerative amplifier, attenuated to approximately 1 μJ energy per pulse, on a 1 mm sapphire plate were used a probe pulses. The white-light continuum pulses had a variable delay with respect to pump pulses (394 nm wavelength, 150 fs-long). Pump and probe beams were focused on a 1 mm quartz cuvette filled with nanocrystals dispersed in toluene. The cumulative effect of spectral chirp and wavefront distortion of laser pulses resulted in a 200-fs time-delay resolution. Optical spectra were recorded with a CCD camera (Andor Newton. 16 bit resolution, used in vertical binning) coupled to a grating spectrometer (Acton SP2300i, equipped with a grating 300 groves/mm). Differential transmission

$\Delta T/T = (T_{on} - T_{off})/T_{off}$ was obtained by recording sequential transmission spectra with (T_{on}) and without (T_{off}) pump pulses illuminating the sample.

The exciting source for the cw-differential transmission spectroscopy was the second harmonic of a Nd:YLF laser (B.M.I., 600) operating at a repetition rate of 1 kHz and emitting 0.4 s-long pulses (hν = 2.36 eV). The cw-emission of a xenon lamp was used as a probe light source. Differential transmission ΔT was detected by a look-in amplifier (SRS, SR830 DSP) triggered by the output of the pump laser. The lifetime of the nonlinear signal was determined by measuring the temporal evolution of the differential transmitted signal of the cw-probe through an oscilloscope (Tektronix, TDS 3054 B) synchronized with the pump pulse train.

The Bi_2S_3 nanowires were synthesized an oleylamine-based procedure. All reagents were obtained from Sigma-Aldrich and were used as received. A mixture of bismuth acetate (3.2 mmol) and oleylamine (OAm, 4,2 ml) was stirred and heated to 130°C over the course of 30 min and then kept at the same temperature for 30 min, under Ar atmosphere. A solution of 15,3 mmol of sulfur dissolved in 10 ml of OAm was quickly injected in the flask. After 30 min at 100°C the reaction was quenched with cold toluene. Unsolubilized materials were removed by centrifugation. Then, acetone was added to the supernatant until it became turbid and the mixture was centrifuged, the supernatant discarded and the precipitated nanocrystals redispersed in toluene. For the TEM observations, the stable Bi_2S_3-toluene dispersions are directly dropped on carbon-coated copper grids. TEM and HRTEM images were obtained with a JEOL 2010 HRTEM equipped with a Gatan Energy Filter (GIF) with a 15 eV window and a 794 slow scan CCD camera.

5

Conclusions

This work provides a quantitative understanding of key materials science issues concerning Bi_2S_3 nanostructures, a non-toxic semiconductor representative of the general class of pnictogen chalcogenides of the type $[Pn_4Ch_6]_n$ with considerable interest for solar energy conversion.

First, the structural and electronic properties of the bulk Bi_2S_3 were investigated. The atomic relaxation of the Bi_2S_3 crystal structure was studied by means of DFT-GGA simulations and provided a good agreement with experimental data. The lattice parameter along the y-direction is practically unchanged, while a small expansion and contraction is observed along the x and z-direction, respectively. In good agreement with the experiments, a direct gap of 1.4 eV was calculated. The band dispersion and the position of the band gap in the Brillouin zone (BZ) are in agreement with those reported in previous theoretical studies. (122) The effective mass of the electrons along the x, y and z-direction was calculated, obtaining $m_x^*/m_e = 3.4$, $m_y^*/m_e = 0.8$, $m_z^*/m_e = 2.1$. This confirms higher mobility and larger electronic coupling of the electrons along the ribbon axis. The inter-ribbon interaction in the x-z plane, is lower along the x-direction than along the z-direction. A confirmation comes from the analysis of the charge density of the system, which shows a charge coupling along the z-direction but not along the x-direction. The decomposition of the density of states into the bismuth and sulfur contribution reveals a predominance of the sulfur component for the valence states, and an almost equal contribution of the sulfur and bismuth components for what concerns the conduction states. The study of the effect of vacancies

on the electronic structure of Bi_2S_3 shows that sulfur vacancies generate doubly occupied states that lie deep in the band gap while bismuth vacancies generate half-empty states a few tens of meV above the VB. This suggests that the sulfur vacancies are responsible for the absence of photoluminescence reported in several experimental investigation on Bi_2S_3.

Concerning the study of the Bi_2S_3 nanostructures, the single ribbon model was adopted to study the effects of relaxation and saturation on finite size systems. For relaxed nanocrystals, the quantum confinement effect is hidden by the persistence of defects on the ribbon edges. In particular, only the ribbons longer than 2 nm were able to reconstruct their surface in order to efficiently passivate electronic trap states. For all lengths, a tensile strain of the ribbon with respect to the periodic system was observed. An investigation of the quantum confinement by keeping the nanocrystals in their experimental geometry and saturating the dangling bonds by means of hydrogen atoms and OH groups was also performed. The dependence of the band gap as a function of the ribbon length L was found to be a power law $L^{-\alpha}$ with $\alpha = 2$. The DFT calculations were performed with two different functionals (PBE and B3LYP), and in all cases, the trends were in good agreement with each other. The TDDFT estimates a band gap of 1.5 eV for long ribbons, that lies in between the experimental range reported in literature (1.2-1.7 eV). Such band gap ideally increases up to 2.2 eV for nanostructures of length $\sim$1 nm. The isostructural material Sb_2S_3 was also studied in comparison with Bi_2S_3. The conclusion is that bismuth sulfide shows a better capability to reconstruct its surfaces with respect to stibnite. Overall the above results suggest that, from the theoretical point of view, the environmental friendly bismuthinite is a valid alternative to the toxic stibnite, as far as concerns of confinement, optical and electronic properties.

The second part of the investigation on Bi_2S_3 nanostructures concerns the structure, stability and electronic properties of ultrathin nanowires. It was demonstrated that such nanostructures are energetically stable at room temperature. In good agreement with the theoretical predictions, ultrathin crystalline Bi_2S_3 nanostructures were in fact synthesized by means of a non-toxic colloidal route. The TEM analysis revealed nanostructures with diameters down to 3 nm that extend for 300 nm along the [010] crystallographic direction with a coherence

length of about 30 nm. Electronic properties were further investigated theoretically. The surface of the nanowires induces intragap doubly-occupied states 300 meV above the valence band and associated to the sulfur atoms of the NWs edges. Due to the peculiar crystalline structure of Bi_2S_3 such defects can be described as 1D-like surface states extending along the nanowires axes. The removal of the edge sulfur atoms is not beneficial for the system since the surface vacancies give rise to doubly-occupied intragap states placed around 250 meV below the conduction band minimum. Intragap states can instead be removed by passivating the surface of the nanowires with carboxylic and amine groups. Calculations showed that both groups are able to eliminate the surface states. In particular, small molecules such as acetic acid and methylamine, can fully passivate all the defective sites at the NWs surface. This suggests a possible route for improving the optoelectronic properties of Bi_2S_3 nanostructures by using shorter molecules and by tuning the ligand size.

The present Thesis clarifies the key issues of Bi_2S_3 materials and provides, to the best of our knowledge, the first theoretical investigation on its nanostructures. The results clarify the morphology and energetics of the nanostructures, the relevance of quantum confinement effects, the role of surfaces and the corresponding electronic states. In particular, the work highlights the tendency of the material to form intragap states that affect the optoelectronic properties, explaining the absence of photoluminescence and showing the necessity to reduce surface defects to increase the technological impact of Bi_2S_3.

References

[1] **Scanning electron microscope image of 100 nm stabilized gold nanoparticles**. http://www.cytodiagnostics.com/store/pc/100nm-Stabilized-Gold-Nanoparticles-20ml-p21.htm. vii, 1

[2] J. A. Chang, J. H. Rhee, S. H. Im, Y. H. Lee, H.-J. Kim, S. I. Seok, M. K. Nazeeruddin, and M. Gratzel. **High-Performance Nanostructured Inorganic-Organic Heterojunction Solar Cells**. *Nano Lett.*, **10**(7):2609–2612, 2010. PMID: 20509686. vii, 7, 8

[3] C. B. Murray, C. R. Kagan, and M. G. Bawendi. **SYNTHESIS AND CHARACTERIZATION OF MONODISPERSE NANOCRYSTALS AND CLOSE-PACKED NANOCRYSTAL ASSEMBLIES**. *Annu. Rev. Mater. Sci.*, **30**(1):545–610, 2000. vii, 21

[4] **Powder X-ray Diffraction**. http://chemwiki.ucdavis.edu/Analytical_Chemistry/Instrumental_Analysis/Diffraction/Powder_X-ray_Diffraction. vii, 23

[5] **X-ray Powder diffraction**. http://serc.carleton.edu/research_education/geochemsheets/techniques/XRD.html. vii, 23

[6] **Pump-probe Spectroscopy**. http://www.unitus.it/biophysics/ricercaen_file/Spectroscopy_file/Pump-probe.htm. viii, 24

[7] A. P. Alivisatos. *Science*, **271**(5251), 1996. 4

[8] D. D. D. Ma, C. S. Lee, F. C. K. Au, S. Y. Tong, and S. T. Lee. **Small-Diameter Silicon Nanowire Surfaces**. *Science*, **299**(5614):1874–1877, 2003. 4, 6

[9] Z. L. Wang and J. H. Song. *Science*, **312**(242), 2006. 4, 7

[10] Y. Wang and G. Cao. **Developments in Nanostructured Cathode Materials for High-Performance Lithium-Ion Batteries**. *Adv. Mater.*, **20**(12):2251–2269, 2008. 4

[11] Y. Wu, C. Wadia, W. Ma, B. Sadtler, and A. P. Alivisatos. **Synthesis and Photovoltaic Application of Copper(I) Sulfide Nanocrystals**. *Nano Lett.*, **8**(8):2551–2555, 2008. PMID: 18651779. 4, 5

[12] T. Li, Y. Lee, and H. Teng. **CuInS2 quantum dots coated with CdS as high-performance sensitizers for TiO2 electrodes in photoelectrochemical cells**. *J. Mater. Chem.*, **21**:5089–5098, 2011. 4, 5

[13] M. J. Bierman and S. Jin. **Potential applications of hierarchical branching nanowires in solar energy conversion**. *Energy Environ. Sci.*, **2**:1050–1059, 2009. 4

[14] J. Liu and D. Xue. **Rapid and scalable route to CuS biosensors: a microwave-assisted Cu-complex transformation into CuS nanotubes for ultrasensitive nonenzymatic glucose sensor**. *J. Mater. Chem.*, **21**:223–228, 2011. 4

[15] D. Moore and Z. L. Wang. **Growth of anisotropic one-dimensional ZnS nanostructures**. *J. Mater. Chem.*, **16**:3898–3905, 2006. 4

[16] X.S. Fang, Y. Bando, G.Z. Shen, C.H. Ye, U.K. Gautam, P.M.F.J. Costa, C.Y. Zhi, C.C. Tang, and D. Golberg. **Ultrafine ZnS Nanobelts as Field Emitters**. *Adv. Mater.*, **19**(18):2593–2596, 2007. 4

[17] Y. Jiang, W.J. Zhang, J.S. Jie, X.M. Meng, J.A. Zapien, and S.-T. Lee. **Homoepitaxial Growth and Lasing Properties of ZnS Nanowire and Nanoribbon Arrays**. *Adv. Mater.*, **18**(12):1527–1532, 2006. 4

[18] C. Mao, D. J. Solis, B. D. Reiss, S. T. Kottmann, R. Y. Sweeney, A. Hayhurst, G. Georgiou, B. Iverson, and A. M. Belcher. **Virus-Based Toolkit for the Directed Synthesis of Magnetic and Semiconducting Nanowires**. *Science*, **303**(5655):213–217, 2004. 4

[19] M. Aresti, M. Saba, R. Piras, D. Marongiu, G. Mula, F. Quochi, A. Mura, C. Cannas, M. Mureddu, A. Ardu, G. Ennas, V. Calzia, A. Mattoni, A. Musinu, and G. Bongiovanni. **Colloidal Bi2S3 Nanocrystals: Quantum Size Effects and Midgap States**. *Adv. Funct. Mater.*, **24**(22):3341–3350, 2014. 4, 29, 33, 46, 57, 59, 61

[20] R. Piras. *J. Phys. Conf. Ser.*, **566**(012017), 2014. 4

[21] L. Li, P. Wu, X. Fang, T. Zhai, L. Dai, M. Liao, Y. Koide, H. Wang, Y. Bando, and D. Golberg. **Single-Crystalline CdS Nanobelts for Excellent Field-Emitters and Ultrahigh Quantum-Efficiency Photodetectors**. *Adv. Mater.*, **22**(29):3161–3165, 2010. 4, 5

[22] C.-H. Lai, M.-Y. Lu, and L.-J. Chen. **Metal sulfide nanostructures: synthesis, properties and applications in energy conversion and storage**. *J. Mater. Chem.*, **22**:19–30, 2012. 4, 6

[23] L. W. Yin and S. T. Lee. **Wurtzite-Twinning-Induced Growth of Three-Dimensional II-VI Ternary Alloyed Nanoarchitectures and their Tunable Band Gap Energy Properties**. *Nano Lett.*, **9**(3):957–963, 2009. 4

[24] Y. Liu, J. A. Zapien, Y. Y. Shan, C.-Y. Geng, C. S. Lee, and S.-T. Lee. **Wavelength-Controlled Lasing in Znx-CdxS Single-Crystal Nanoribbons**. *Adv. Mater.*, **17**(11):1372–1377, 2005. 4

REFERENCES

[25] V. J. Gandubert, E. Torres, and C. M. Niemeyer. **Investigation of cytochrome P450-modified cadmium sulfide quantum dots as photocatalysts**. *J. Mater. Chem.*, **18**:3824–3830, 2008. 4

[26] M. Muruganandham and Y. Kusumoto. **Synthesis of N, C Codoped Hierarchical Porous Microsphere ZnS As a Visible Light-Responsive Photocatalyst**. *J. Phys. Chem. C*, **113**(36):16144–16150, 2009. 4

[27] M.Y. Lu, M.P. Lu, Y.-A. Chung, M.J. Chen, Z. L. Wang, and L.J. Chen. **Intercrossed Sheet-Like Ga-Doped ZnS Nanostructures with Superb Photocatalytic Actvitiy and Photoresponse**. *J. Phys. Chem. C*, **113**(29):12878–12882, 2009. 4

[28] X. Fang, Y. Bando, M. Liao, U. K. Gautam, C. Zhi, B. Dierre, B. Liu, T. Zhai, T. Sekiguchi, Y. Koide, and D. Golberg. **Single-Crystalline ZnS Nanobelts as Ultraviolet-Light Sensors**. *Adv. Mater.*, **21**(20):2034–2039, 2009. 5

[29] E. Monroy et al. **Wide-bandgap semiconductor ultraviolet photodetectors**. *Semicond. Sci. Technol.*, **18**(4), 2003. 5

[30] T. C. Harman, P. J. Taylor, M. P. Walsh, and B. E. LaForge. **Quantum Dot Superlattice Thermoelectric Materials and Devices**. *Science*, **297**(5590):2229–2232, 2002. 5

[31] R. Malakooti, L. Cademartiri, A. Migliori, and G. A. Ozin. **Ultrathin Sb2S3 nanowires and nanoplatelets**. *J. Mater. Chem.*, **18**:66–69, 2008. 5, 6, 8

[32] L. D. Hicks and M. S. Dresselhaus. **Effect of quantum-well structures on the thermoelectric figure of merit**. *Phys. Rev. B*, **47**:12727–12731, May 1993. 5

[33] J. Seo, J. Jang, S. Park, C. Kim, B. Park, and J. Cheon. **Two-Dimensional SnS2 Nanoplates with Extraordinary High Discharge Capacity for Lithium Ion Batteries**. *Adv. Mater.*, **20**(22):4269–4273, 2008. 5

[34] C. M. Grgicak and J. B. Giorgi. **Improved Performance of Ni- and Co-YSZ Anodes via Sulfidation to NiS- and CoS-YSZ. Effects of Temperature on Electrokinetic Parameters**. *J. Phys. Chem. C*, **111**(42):15446–15455, 2007. 5

[35] P. Millet, F. Andolfatto, and R. Durand. **Design and performance of a solid polymer electrolyte water electrolyzer**. *Int. J. Hydrogen Energ.*, **21**(2):87 – 93, 1996. 5

[36] D. Merki, S. Fierro, H. Vrubel, and X. Hu. **Amorphous molybdenum sulfide films as catalysts for electrochemical hydrogen production in water**. *Chem. Sci.*, **2**:1262–1267, 2011. 5

[37] J. Chen et al. **Electrochemical hydrogen storage in MoS2 nanotubes**. *J. Am. Chem. Soc.*, **123**:11813, 2001. 5

[38] B. Zhang, X. Ye, W. Hou, Y. Zhao, and Y. Xie. **Biomolecule-Assisted Synthesis and Electrochemical Hydrogen Storage of Bi2S3 Flowerlike Patterns with Well-Aligned Nanorods**. *J. Phys. Chem. B*, **110**(18):8978–8985, 2006. PMID: 16671704. 5

[39] X. Li, H. Shen, S. Li, J. Z. Niu, H. Wang, and L. S. Li. **Investigation on type-II Cu2S-CdS core/shell nanocrystals: synthesis and characterization**. *J. Mater. Chem.*, **20**:923–928, 2010. 5

[40] M. Page, O. Niitsoo, Y. Itzhaik, D. Cahen, and G. Hodes. **Copper sulfide as a light absorber in wet-chemical synthesized extremely thin absorber (ETA) solar cells**. *Energy Environ. Sci.*, **2**:220–223, 2009. 5

[41] D. B. Mitzi, M. Yuan, W. Liu, A. J. Kellock, S. J. Chey, V. Deline, and A. G. Schrott. **A High-Efficiency Solution-Deposited Thin-Film Photovoltaic Device**. *Adv. Mater.*, **20**(19):3657–3662, 2008. 5

[42] M. G. Panthani, V. Akhavan, B. Goodfellow, J. P. Schmidtke, L. Dunn, A. Dodabalapur, P. F. Barbara, and B. A. Korgel. **Synthesis of CuInS2, CuInSe2, and Cu(InxGa1-x)Se2 (CIGS) Nanocrystal Inks for Printable Photovoltaics**. *J. Am. Chem. Soc.*, **130**(49):16770–16777, 2008. PMID: 19049468. 5

[43] Y. K. A. Lau, Davin J. Chernak, Matthew J. Bierman, and S. Jin. **Epitaxial growth of hierarchical PbS nanowires**. *J. Mater. Chem.*, **19**:934–940, 2009. 5

[44] F. Zhang and S. S. Wong. **Controlled Synthesis of Semiconducting Metal Sulfide Nanowires**. *Chem. Mater.*, **21**(19):4541–4554, 2009. 5

[45] Y. Hu, Z. Zheng, H. Jia, Y. Tang, and L. Zhang. **Selective Synthesis of FeS and FeS2 Nanosheet Films on Iron Substrates as Novel Photocathodes for Tandem Dye-Sensitized Solar Cells**. *J. Phys. Chem. C*, **112**(33):13037–13042, 2008. 6

[46] H. Sun, D. Qin, S. Huang, X. Guo, D. Li, Y. Luo, and Q. Meng. **Dye-sensitized solar cells with NiS counter electrodes electrodeposited by a potential reversal technique**. *Energy Environ. Sci.*, **4**:2630–2637, 2011. 6

[47] C. L. Stender, E. C. Greyson, Y. Babayan, and T. W. Odom. **Patterned MoS2 Nanostructures Over Centimeter-Square Areas**. *Adv. Mater.*, **17**(23):2837–2841, 2005. 6

[48] M. T. Spitler and B. A. Parkinson. **Dye sensitization of single crystal semiconductor electrodes**. *Acc. Chem. Res.*, **42**(12):2017–29, 2009. 6

[49] Y.-F. Lin, J. Song, Y. Ding, S.-Y. Lu, and Z. L. Wang. **Piezoelectric nanogenerator using CdS nanowires**. *Appl. Phys. Lett.*, **92**(2):–, 2008. 6

[50] Y.-F. Lin, J. Song, Y. Ding, S.-Y. Lu, and Z. L. Wang. **Alternating the Output of a CdS Nanowire Nanogenerator by a White-Light-Stimulated Optoelectronic Effect**. *Adv. Mater.*, **20**(16):3127–3130, 2008. 6

[51] M. Law, L. E. Greene, J. C. Johnson, R. Saykally, and P. D. Yang. *Nat. Mater.*, **4**(455), 2005. 6

[52] K. C. Chen, W. W. Wu, C. N. Liao, L. J. Chen, and K. N. Tu. *Science*, **321**(1066), 2008. 6

[53] C. Lai, K. Huang, J. Cheng, C. Lee, B. Hwang, and L. Chen. **Direct growth of high-rate capability and high capacity copper sulfide nanowire array cathodes for lithium-ion batteries**. *J. Mater. Chem.*, **20**:6638–6645, 2010. 6

[54] Z. Wen and J. Li. **Hierarchically structured carbon nanocomposites as electrode materials for electrochemical energy storage, conversion and biosensor systems**. *J. Mater. Chem.*, **19**:8707–8713, 2009. 6

[55] K. W. Huang, J. H. Wang, H. C. Chen, H. C. Hsu, Y. C. Chang, M. Y. Lu, C. Y. Lee, and L. J. Chen. *J. Mater. Chem.*, **17**:2307, 2007. 6

[56] R. J. Mehta, C. Karthik, W. Jiang, B. Singh, Y. Shi, R. W. Siegel, T. Borca-Tasciuc, and G. Ramanath. **High Electrical Conductivity Antimony Selenide Nanocrystals and Assemblies**. *Nano Lett.*, **10**(11):4417–4422, 2010. PMID: 20925405. 6, 7, 8

[57] L. Cademartiri, R. Malakooti, P. G. O'Brien, A. Migliori, S. Petrov, N. P. Kherani, and G. A. Ozin. **Large-Scale Synthesis of Ultrathin Bi2S3 Necklace Nanowires**. *Angew. Chem. Int. Edit.*, **47**(20):3814–3817, 2008. 6, 8, 33, 51, 59

[58] Z. Deng, M. Mansuripur, and A. J. Muscat. **Simple Colloidal Synthesis of Single-Crystal Nanotubes with Composition Dependent Band-Gap Energy in the Near-Infrared**. *Nano Lett.*, **9**(5):2015–2020, 2009. 6, 8

[59] J. Varghese, S. Barth, L. Keeney, R. W. Whatmore, and J. D. Holmes. **Nanoscale Ferroelectric and Piezoelectric Properties of Sb2S3 Nanowire Arrays**. *Nano Lett.*, **12**(2):868–872, 2012. PMID: 22268546. 6

[60] M. Ieong, B. Doris, J. Kedzierski, K. Rim, and M. Yang. **Silicon Device Scaling to the Sub-10-nm Regime**. *Science*, **306**(5704):2057–2060, 2004. 6

[61] X. Tu, S. Manohar, A. Jagota, and M. Zheng. **DNA sequence motifs for structure-specific recognition and separation of carbon nanotubes**. *Nature*, **460**(7252):250–253, Jul 2009. 6

[62] M. Zheng, A. Jagota, M. S. Strano, A. P. Santos, P. Barone, S. G. Chou, B. A. Diner, M. S. Dresselhaus, R. S. Mclean, G. B. Onoa, G. G. Samsonidze, E. D. Semke, M. Usrey, and D. J. Walls. **Structure-Based Carbon Nanotube Sorting by Sequence-Dependent DNA Assembly**. *Science*, **302**(5650):1545–1548, 2003. 6

[63] J. D. Holmes, K. P. Johnston, R. C. Doty, and B. A. Korgel. **Control of Thickness and Orientation of Solution-Grown Silicon Nanowires**. *Science*, **287**(5457):1471–1473, 2000. 6

[64] A. B. Greytak, L. J. Lauhon, M. S. Gudiksen, and C. M. Lieber. **Growth and transport properties of complementary germanium nanowire field-effect transistors**. *Appl. Phys. Lett.*, **84**(21), 2004. 6

[65] R. G. Hobbs, S. Barth, N. Petkov, M. Zirngast, C. Marschner, M. A. Morris, and J. D. Holmes. **Seedless Growth of Sub-10 nm Germanium Nanowires**. *J. Am. Chem. Soc.*, **132**(39):13742–13749, 2010. PMID: 20836555. 6

[66] Y. Cai, S. K. Chan, I. K. Sou, Y. F. Chan, D. S. Su, and N. Wang. **The Size-Dependent Growth Direction of ZnSe Nanowires**. *Adv. Mater.*, **18**(1):109–114, 2006. 6

[67] Y. Kim, H. J. Joyce, Q. Gao, H. H. Tan, C. Jagadish, M. Paladugu, J. Zou, and A. A. Suvorova. **Influence of Nanowire Density on the Shape and Optical Properties of Ternary InGaAs Nanowires**. *Nano Lett.*, **6**(4):599–604, 2006. PMID: 16608251. 6

[68] Z. Wu, J. B. Neaton, and J. C. Grossman. **Quantum Confinement and Electronic Properties of Tapered Silicon Nanowires**. *Phys. Rev. Lett.*, **100**:246804, Jun 2008. 7

[69] P. Yang, R. Yan, and M. Fardy. **Semiconductor Nanowire: What's Next?** *Nano Lett.*, **10**(5):1529–1536, 2010. PMID: 20394412. 7

[70] Z. Huang, X. Zhang, M. Reiche, L. Liu, W. Lee, T. Shimizu, S. Senz, and U. Gösele. **Extended Arrays of Vertically Aligned Sub-10 nm Diameter [100] Si Nanowires by Metal-Assisted Chemical Etching**. *Nano Lett.*, **8**(9):3046–3051, 2008. PMID: 18698834. 7

[71] H. Adhikari, A. F. Marshall, C. E. D. Chidsey, and P. C. McIntyre. **Germanium Nanowire Epitaxy: Shape and Orientation Control**. *Nano Lett.*, **6**(2):318–323, 2006. PMID: 16464057. 7

[72] X. Li, X. Wang, L. Zhang, S. Lee, and H. Dai. **Chemically Derived, Ultrasmooth Graphene Nanoribbon Semiconductors**. *Science*, **319**(5867):1229–1232, 2008. 7

[73] L. Jiao, L. Zhang, X. Wang, G. Diankov, and H. Dai. **Narrow graphene nanoribbons from carbon nanotubes**. *Nature*, **458**(7240):877–880, Apr 2009. 7

[74] L. Jiao, X. Wang, G. Diankov, H. Wang, and H. Dai. **Facile synthesis of high-quality graphene nanoribbons**. *Nat. Nano.*, **5**(5):321–325, May 2010. 7

[75] X. Wang and H. Dai. **Etching and narrowing of graphene from the edges**. *Nat. Chem.*, **2**(8):661–665, Aug 2010. 7

[76] J. Cai, P. Ruffieux, R. Jaafar, M. Bieri, T. Braun, S. Blankenburg, M. Muoth, A. P. Seitsonen, M. Saleh, X. Feng, K. Mullen, and R. Fasel. **Atomically precise bottom-up fabrication of graphene nanoribbons**. *Nature*, **466**(7305):470–473, Jul 2010. 7

REFERENCES

[77] X. Wang, Y. Ouyang, X. Li, H. Wang, J. Guo, and H. Dai. **Room-Temperature All-Semiconducting Sub-10-nm Graphene Nanoribbon Field-Effect Transistors**. *Phys. Rev. Lett.*, **100**:206803, May 2008. 7

[78] M. Y. Han, B. Özyilmaz, Y. Zhang, and P. Kim. **Energy Band-Gap Engineering of Graphene Nanoribbons**. *Phys. Rev. Lett.*, **98**:206805, May 2007. 7

[79] M. Evaldsson, I. V. Zozoulenko, Hengyi Xu, and T. Heinzel. **Edge-disorder-induced Anderson localization and conduction gap in graphene nanoribbons**. *Phys. Rev. B*, **78**:161407, Oct 2008. 7

[80] J. A. Rogers. **Nanoelectronics: Nanoribbons on the edge**. *Nat. Nano.*, **5**(10):698–699, Oct 2010. 7

[81] F. Schwierz. **Graphene transistors**. *Nat. Nano.*, **5**(7):487–496, Jul 2010. 7

[82] H. Chang, B. Sarkar, and C. W. Liu. **Synthesis of Sb2Se3 Nanowires via a Solvothermal Route from the Single Source Precursor Sb[Se2P(OiPr)2]3**. *Cryst. Growth Des.*, **7**(12):2691–2695, 2007. 7

[83] W. Farfán, E. Mosquera, R. Vadapoo, S. Krishnan, and C. Marín. *J. Nanosci. Nanotechno.*, **10**(9):5847–5850, 2010. [link]. 7

[84] Y. Yu, R. H. Wang, Q. Chen, and L.-M. Peng. **High-Quality Ultralong Sb2Se3 and Sb2S3 Nanoribbons on a Large Scale via a Simple Chemical Route**. *J. Phys. Chem. B*, **110**(27):13415–13419, 2006. PMID: 16821864. 7

[85] L. Guo, G. Ji, X. Chang, M. Zheng, Y. Shi, and Y. Zheng. **Microwave-assisted synthesis of Sb 2 Se 3 submicron tetragonal tubular and spherical crystals**. *Nanotechnology*, **21**(3):035606, 2010. 7

[86] Qiaofeng Han, Liang Chen, Meijuan Wang, Xujie Yang, Lude Lu, and Xin Wang. % bf Low-temperature synthesis of uniform Sb2S3 nanorods and its visible-light-driven photocatalytic activities. *Mater. Sci. and Eng B*, **166**(1):118 – 121, 2010. 7

[87] K. H. Park, J. Choi, H. J. Kim, J. B. Lee, and S. U. Son. **Synthesis of Antimony Sulfide Nanotubes with Ultrathin Walls via Gradual Aspect Ratio Control of Nanoribbons**. *Chem. Mater.*, **19**(16):3861–3863, 2007. 7

[88] R. B. Yang, J. Bachmann, E. Pippel, A. Berger, J. Woltersdorf, U. Gösele, and K. Nielsch. **Pulsed Vapor-Liquid-Solid Growth of Antimony Selenide and Antimony Sulfide Nanowires**. *Adv. Mater.*, **21**(31):3170–3174, 2009. 7

[89] R. B. Yang, N. Zakharov, O. Moutanabbir, K. Scheerschmidt, L. Wu, U. Gösele, J. Bachmann, and K. Nielsch. **The Transition between Conformal Atomic Layer Epitaxy and Nanowire Growth**. *J. Am. Chem. Soc.*, **132**(22):7592–7594, 2010. PMID: 20469861. 7

[90] S. Moon, Y. Itzhaik, J. Yum, S. M. Zakeeruddin, G. Hodes, and M. Grätzel. **Sb2S3-Based Mesoscopic Solar Cell using an Organic Hole Conductor**. *J. Phys. Chem. Lett.*, **1**(10):1524–1527, 2010. 7

[91] T. Zhai, M. Ye, L. Li, X. Fang, M. Liao, Y. Li, Y. Koide, Y. Bando, and D. Golberg. **Single-Crystalline Sb2Se3 Nanowires for High-Performance Field Emitters and Photodetectors**. *Adv. Mater.*, **22**(40):4530–4533, 2010. 7

[92] J. A. Chang, S. H. Im, Y. H. Lee, H.-J. Kim, C.-S. Lim, J. H. Heo, and S. I. Seok. **Panchromatic Photon-Harvesting by Hole-Conducting Materials in Inorganic-Organic Heterojunction Sensitized-Solar Cell through the Formation of Nanostructured Electron Channels**. *Nano Lett.*, **12**(4):1863–1867, 2012. PMID: 22401668. 7

[93] N. Guijarro, T. Lutz, T. Lana-Villarreal, F. O Mahony, R. Gómez, and S. A. Haque. **Toward Antimony Selenide Sensitized Solar Cells: Efficient Charge Photogeneration at spiro-OMeTAD/Sb2Se3/Metal Oxide Heterojunctions**. *J. Phys. Chem. Lett.*, **3**(10):1351–1356, 2012. 7, 8

[94] Rath et al. **Solution-processed inorganic bulk nano-heterojunctions and their application to solar cells**. *Nat. Photon.*, **6**(8):529–534, Aug 2012. 7, 62

[95] B. O'Regan and M. Gratzel. **A low-cost, high-efficiency solar cell based on dye-sensitized colloidal TiO2 films**. *Nature*, **353**(6346):737–740, Oct 1991. 7

[96] G. Hodes. **Comparison of Dye- and Semiconductor-Sensitized Porous Nanocrystalline Liquid Junction Solar Cells**. *J. Phys. Chem. C*, **112**(46):17778–17787, 2008. 7

[97] T. Lutz, A. MacLachlan, A. Sudlow, J. Nelson, M. S. Hill, K. C. Molloy, and S. A. Haque. **Thermal decomposition of solution processable metal xanthates on mesoporous titanium dioxide films: a new route to quantum-dot sensitised heterojunctions**. *Phys. Chem. Chem. Phys.*, **14**:16192–16196, 2012. 8

[98] C.H. Bhosale, M.D. Uplane, P.S. Patil, and C.D. Lockhande. **Preparation and properties of sprayed antimony trisulphide films**. *Thin Solid Films*, **248**(2):137 – 139, 1994. 8

[99] M. Y. Versavel and J. A. Haber. % bf Structural and optical properties of amorphous and crystalline antimony sulfide thin-films. *Thin Solid Films*, **515**(18):7171 – 7176, 2007. 8

[100] C. D. Lokhande, B. R. Sankapal, R. S. Mane, H. M. Pathan, M. Muller, M. Giersig, and V. Ganesan. % bf XRD, SEM, AFM, HRTEM, {EDAX} and {RBS} studies of chemically deposited Sb2S3 and Sb2Se3 thin films. *Appl. Surf. Sci.*, **193**(14):1 – 10, 2002. 8

[101] H. Maghraoui-Meherzi, T. Ben Nasr, N. Kamoun, and M. Dachraoui. % bf Structural, morphology and optical properties of chemically deposited Sb2S3 thin films. *Physica B*, **405**(15):3101 – 3105, 2010. 8

[102] S. Rühle, M. Shalom, and A. Zaban. **Quantum-Dot-Sensitized Solar Cells**. *ChemPhysChem*, **11**(11):2290–2304, 2010. 8

[103] Q. Han, S. Sun, D. Sun, J. Zhu, and X. Wang. **Room-temperature synthesis from molecular precursors and photocatalytic activities of ultralong Sb2S3 nanowires**. *RSC Adv.*, **1**:1364–1369, 2011. 8

[104] L. Cademartiri, G. Guerin, K. J. M. Bishop, M. A. Winnik, and G. A. Ozin. **Polymer-like Conformation and Growth Kinetics of Bi2S3 Nanowires**. *J. Am. Chem. Soc.*, **134**(22):9327–9334, 2012. PMID: 22533703. 8

[105] H. Bao, X. Cui, C. M. Li, Q. Song, Z. Lu, and J. Guo. **Synthesis and Electrical Transport Properties of Single-Crystal Antimony Sulfide Nanowires**. *J. Phys. Chem. C*, **111**(45):17131–17135, 2007. 8

[106] M.E. Rincn, M. Snchez, P.J. George, A. Snchez, and P.K. Nair. % bf Comparison of the Properties of Bismuth Sulfide Thin Films Prepared by Thermal Evaporation and Chemical Bath Deposition. *J. Solid State Chem.*, **136**(2):167 – 174, 1998. 8

[107] F. Perales, G. Lifante, F. Agulló-Rueda, and C. de las Heras. **Optical and structural properties in the amorphous to polycrystalline transition in Sb 2 S 3 thin films**. *J. Phys. D*, **40**(8):2440, 2007. 8

[108] A.G. Vedeshwar. **Optical Properties of Amorphous and Polycrystalline Stibnite (Sb_2S_3) Films**. *J. Phys. III France*, **5**(8):1161–1172, 1995. 8

[109] A.M. Karguppikar and A.G. Vedeshwar. **Thickness dependence of the forbidden energy gap in stibnite (Sb2S3) thin films**. *Phys. Lett. A*, **126**(2):123 – 126, 1987. 8

[110] E. Y. Atabaeva, S. A. Mashkov, and S. V. Popova. *Krystallografiya*, **18**(173), 1974. 9

[111] H. Okamoto. **The Bi-Se (Bismuth-Selenium) System**. *J. Phase Equilib.*, **15**(2):195–201, 1994. 9

[112] N.S. Yesugade, C.D. Lokhande, and C.H. Bhosale. **Structural and optical properties of electrodeposited Bi2S3, Sb2S3 and As2S3 thin films**. *Thin Solid Films*, **263**(2):145 – 149, 1995. 9, 11

[113] J. Lukose and B. Pradeep. **Electrical and optical properties of bismuth sulphide [Bi2S3] thin films prepared by reactive evaporation**. *Solid State Commun.*, **78**(6):535 – 538, 1991. 9, 11

[114] S. Mahmoud, A. H. Eid, and H. Omar. *Fizika A*, **6**(111), 1997. 9, 11

[115] I.K. El Zawawi, A. Abdel-Moez, F.S.Terra, and M. Mounir. % bf Substrate temperature effect on the optical and electrical properties of antimony trisulfide thin films. *Thin Solid Films*, **324**(12):300 – 304, 1998. 9

[116] S. Mahanty, J. M. Merino, and M. León. **Preparation and optical studies on flash evaporated Sb2S3 thin films**. *J. Vac. Sci. Technol. A*, **15**(6), 1997. 9

[117] A.P. Torane, K.Y. Rajpure, and C.H. Bhosale. % bf Preparation and characterization of electrodeposited Sb2Se3 thin films. *Mater. Chem. Phys.*, **61**(3):219 – 222, 1999. 9

[118] Y. Rodríguez-Lazcano, Y. Peña, M.T.S. Nair, and P.K. Nair. % bf Polycrystalline thin films of antimony selenide via chemical bath deposition and post deposition treatments. *Thin Solid Films*, **493**(12):77 – 82, 2005. 9

[119] C. E. Patrick and F. Giustino. **Structural and Electronic Properties of Semiconductor-Sensitized Solar-Cell Interfaces**. *Adv. Funct. Mater.*, **21**(24):4663–4667, 2011. 9, 28

[120] R. Caracas and X. Gonze. **First-principles study of the electronic properties of A2B3 minerals, with A=Bi,Sb and B=S,Se**. *Phys. Chem. of Miner.*, **32**(4):295–300, 2005. 9, 27, 34

[121] R. Vadapoo, S. Krishnan, H. Yilmaz, and C. Marin. **Self-Standing Nanoribbons of Antimony Selenide and Antimony Sulfide with Well-Defined Size and Band Gap**. *Nanotechnology*, **22**(17):175705, 2011. 9, 33, 35

[122] P. Larson, V. A. Greanya, W. C. Tonjes, Rong Liu, S. D. Mahanti, and C. G. Olson. **Electronic structure of Bi_2X_3 ($X = \mathrm{S}, \mathrm{Se}, \mathrm{T}$) compounds: Comparison of theoretical calculations with photoemission studies**. *Phys. Rev. B*, **65**:085108, Feb 2002. 9, 28, 52, 65

[123] Y. Sharma, P. Srivastava, A. Dashora, L. Vadkhiya, M.K. Bhayani, R. Jain, A.R. Jani, and B.L. Ahuja. % bf Electronic structure, optical properties and Compton profiles of Bi2S3 and Bi2Se3. *Solid State Sci.*, **14**(2):241 – 249, 2012. 9, 34

[124] H. Koc, A. M. Mamedov, E. Deligoz, and H. Ozisik. % bf First principles prediction of the elastic, electronic, and optical properties of Sb2S3 and Sb2Se3 compounds. *Solid State Sci.*, **14**(8):1211 – 1220, 2012. 9

[125] T. Ben Nasr, H. Maghraoui-Meherzi, H. Ben Abdallah, and R. Bennaceur. % bf Electronic structure and optical properties of Sb2S3 crystal. *Physica B*, **406**(2):287 – 292, 2011. 9

[126] Y. Sharma and P. Srivastava. **First principles Study of Electronic and Optical Properties of Bi2Se3 in its Trigonal and Orthorhombic Phases**. *AIP Conf. Proc.*, **1249**(1), 2010. 9

[127] W. Kohn. **Nobel Lecture: Electronic structure of matter¯wave functions and density functionals**. *Rev. Mod. Phys.*, **71**:1253–1266, Oct 1999. 11, 12

[128] E. Runge and E. K. U. Gross. **Density-Functional Theory for Time-Dependent Systems**. *Phys. Rev. Lett.*, **52**:997–1000, Mar 1984. 12, 17, 62

REFERENCES

[129] P. Giannozzi, S. Baroni, N. Bonini, M. Calandra, R. Car, C. Cavazzoni, D. Ceresoli, G. L. Chiarotti, M. Cococcioni, I. Dabo, A. Dal Corso, S. de Gironcoli, S. Fabris, G. Fratesi, R. Gebauer, U. Gerstmann, C. Gougoussis, A. Kokalj, M. Lazzeri, L. Martin-Samos, N. Marzari, F. Mauri, R. Mazzarello, S. Paolini, A. Pasquarello, L. Paulatto, C. Sbraccia, S. Scandolo, G. Sclauzero, A. P. Seitsonen, A. Smogunov, P. Umari, and R. M. Wentzcovitch. **QUANTUM ESPRESSO: a modular and open-source software project for quantum simulations of materials**. *J. Phys.-Condens. Mat.*, **21**(39):395502 (19pp), 2009. 12, 31, 61

[130] **TURBOMOLE V6.4 2012, a development of University of Karlsruhe and Forschungszentrum Karlsruhe GmbH, 1989-2007, TURBOMOLE GmbH, since 2007; available from** `http://www.turbomole.com`. 12

[131] P. Hohenberg and W. Kohn. **Inhomogeneous Electron Gas**. *Phys. Rev.*, **136**:B864–B871, Nov 1964. 12, 17

[132] J. P. Perdew. **Rationale for mixing exact exchange with density functional approximations**. *J. Chem. Phys*, (105 (22)):9982–9985, 1996. 16, 31, 61

[133] A. D. Becke. **A new mixing of Hartree-Fock and local density-functional theories**. *J. Chem. Phys*, (98 (2)):1372–1377, 1993. 16

[134] P.J. Stephens, F. J. Devlin, C. F. Chabalowski, and M. J. Frisch. **Ab Initio Calculation of Vibrational Absorption and Circular Dichroism Spectra Using Density Functional Force Fields**. *J. Chem. Phys*, (98 (45)):11623–11627, 1994. 16

[135] R. van Leeuwen. **Causality and Symmetry in Time-Dependent Density-Functional Theory**. *Phys. Rev. Lett.*, **80**:1280–1283, Feb 1998. 17

[136] M. Petersilka, U. J. Gossmann, and E. K. U. Gross. **Excitation Energies from Time-Dependent Density-Functional Theory**. *Phys. Rev. Lett.*, **76**:1212–1215, Feb 1996. 17

[137] R. O. Jones and O. Gunnarsson. **The density functional formalism, its applications and prospects**. *Rev. Mod. Phys.*, **61**:689–746, Jul 1989. 18

[138] G. Onida, L. Reining, and A. Rubio. **Electronic excitations: density-functional versus many-body Green's-function approaches**. *Rev. Mod. Phys.*, **74**:601–659, Jun 2002. 18

[139] G. Malloci, L. Chiodo, A. Rubio, and A. Mattoni. **Structural and Optoelectronic Properties of Unsaturated ZnO and ZnS Nanoclusters**. *J. Phys. Chem. C*, **116**(15):8741–8746, 2012. 18

[140] R. O. Jones and O. Gunnarsson. **The density functional formalism, its applications and prospects**. *Rev. Mod. Phys.*, **61**:689–746, July 1989. 18, 38, 62

[141] W. Hofmann. *Z. Kristallogr.*, **86**(225), 1933. 25

[142] Kupčik and Veselá Nováková. **Zur Kristallstruktur des Bismuthinits, Bi_2S_3**. *Tschermaks Mineralogische Petrographische Mitteilunge*, (14):55–59, 1970. 25

[143] A. Kyono and M. Kimata. **Structural variations induced by difference of the inert pair effect in the stibnite-bismuthinite solid solution series $(Sb,Bi)_2S_3$**. *Am. Mineral.*, (89):932–940, 2004. 25

[144] L.F. Lundegaard, E. Makovicky, T. Boffa-Ballaran, and T. Balic-Zunic. **Crystal Structure and Cation Lone Electron Pair Activity of Bi2S3 between 0 and 10GPa**. *Phys. Chem. Miner.*, **32**:578–584, 2005. 26, 27, 31, 34, 61

[145] M. R. Filip, C. E. Patrick, and F. Giustino. *GW* **quasiparticle band structures of stibnite, antimonselite, bismuthinite, and guanajuatite**. *Phys. Rev. B*, **87**:205125, May 2013. 26, 37, 39, 52

[146] M. Dion, H. Rydberg, E. Schröder, D. C. Langreth, and B. I. Lundqvist. **Van der Waals Density Functional for General Geometries**. *Phys. Rev. Lett.*, **92**:246401, Jun 2004. 27

[147] G. Román-Pérez and J. M. Soler. **Efficient Implementation of a van der Waals Density Functional: Application to Double-Wall Carbon Nanotubes**. *Phys. Rev. Lett.*, **103**:096102, Aug 2009. 27

[148] S.-Q. Zhan, H. Wan, L. Xu, W.-Q. Huang, G.-F. Huang, J.-P. Long, and P. Peng. **Native vacancy defects in bismuth sulfide**. *Int. J. Mod. Phys. B*, **28**(23):1450150, 2014. 31

[149] N. Troullier and José Luriaas Martins. **Efficient pseudopotentials for plane-wave calculations**. *Phys. Rev. B*, **43**:1993–2006, Jan 1991. 32, 61

[150] V. Stavila, K. H. Whitmire, and I. Rusakova. **Synthesis of Bi2S3 Nanostructures from Bismuth(III) Thiourea and Thiosemicarbazide Complexes**. *Chem. Mater.*, **21**(22):5456–5465, 2009. 33

[151] X. Zhu, J. Ma, Y. Wang, J. Tao, B. Lin, Y. Ren, X. Jiang, and J. Liu. % bf Morphology-controlled synthesis and characterization of bismuth sulfide crystallites via a hydrothermal method. *Ceram. Int.*, **34**(1):249 – 251, 2008. 33

[152] Z. Quan, J. Yang, P. Yang, Z. Wang, C. Li, and J. Lin. **Facile Synthesis and Characterization of Single Crystalline Bi2S3 with Various Morphologies**. *Cryst. Growth Des.*, **8**(1):200–207, 2008. 33

[153] H.-C. Liao, M.-C. Wu, M.-H. Jao, C.-M. Chuang, Y.-F. Chen, and W.-F. Su. **Synthesis, optical and photovoltaic properties of bismuth sulfide nanorods**. *CrystEngComm*, **14**:3645–3652, 2012. 33

[154] U. V. Kawade, R. P. Panmand, Y. A. Sethi, M. V. Kulkarni, S. K. Apte, S. D. Naik, and B. B. Kale. **Environmentally benign enhanced hydrogen production via lethal H2S under natural sunlight using hierarchical nanostructured bismuth sulfide**. *RSC Adv.*, **4**:49295–49302, 2014. 33

[155] B. Xue, T. Sun, F. Mao, and J. Xie. % bf Gelatin-assisted green synthesis of bismuth sulfide nanorods under microwave irradiation. *Mater. Lett.*, **122**(0):106 – 109, 2014. 33

[156] L. Cademartiri, F. Scotognella, P. G. O'Brien, B. V. Lotsch, J. Thomson, S. Petrov, N. P. Kherani, and G. A. Ozin. **Cross-Linking Bi2S3 Ultrathin Nanowires: A Platform for Nanostructure Formation and Biomolecule Detection**. *Nano Lett.*, **9**(4):1482–1486, 2009. 33

[157] Y. Yu, C. H. Jin, R. H. Wang, Q. Chen, and L.-M. Peng. **High-Quality Ultralong Bi2S3 Nanowires: Structure, Growth, and Properties**. *J. Phys. Chem. B*, **109**(40):18772–18776, 2005. PMID: 16853415. 33

[158] H. Bao, X. Cui, C. M. Li, Y. Gan, J. Zhang, and J. Guo. **Photoswitchable Semiconductor Bismuth Sulfide (Bi2S3) Nanowires and Their Self-Supported Nanowire Arrays**. *J. Phys. Chem. C*, **111**(33):12279–12283, 2007. 33

[159] V. Calzia, G. Malloci, G. Bongiovanni, and A. Mattoni. **Electronic Properties and Quantum Confinement in Bi2S3 Ribbon-Like Nanostructures**. *J. Phys. Chem. C*, **117**(42):21923–21929, 2013. 33

[160] L. F. Lundegaard, R. Miletich, T. Balic-Zunic, and E. Makovicky. **Equation of state and crystal structure of Sb2S3 between 0 and 10 GPa**. *Phys. Chem. Miner.*, **30**:463–468, 2003. 34

[161] M. Graetzel, R. A. J. Janssen, D. B. Mitzi, and E. H. Sargent. **Materials interface engineering for solution-processed photovoltaics**. *Nature*, **488**:304–312, Aug 2012. 10.1038/nature11476. 36

[162] G. Malloci, L. Chiodo, A. Rubio, and A. Mattoni. **Structural and Optoelectronic Properties of Unsaturated ZnO and ZnS Nanoclusters**. *J. Phys. Chem. C*, **116**(15):8741–8746, 2012. 36, 62

[163] M. K. Armbruster, F. Weigend, C. van Wullen, and W. Klopper. **Self-consistent treatment of spin-orbit interactions with efficient Hartree-Fock and density functional methods**. *Phys. Chem. Chem. Phys.*, **10**:1748–1756, 2008. 37, 61

[164] B. Metz, H. Stoll, and M. Dolg. **Small-core multiconfiguration-Dirac–Hartree–Fock-adjusted pseudopotentials for post-[bold d] main group elements: Application to PbH and PbO**. *J. Chem. Phys.*, **113**(7):2563–2569, 2000. 37, 62

[165] A. Cantarero, J. Martinez-Pastor, A. Segura, and A. Chevy. **Excitonic absorption and Urbach's tail in bismuth sulfide single crystals**. *Appl Phys A*, **45**(2):125–132, 1988. 46

[166] C. B. Murray, D. J. Norris, and M. G. Bawendi. **Synthesis and characterization of nearly monodisperse CdE (E = sulfur, selenium, tellurium) semiconductor nanocrystallites**. *J. Am. Chem. Soc.*, **115**(19):8706–8715, 1993. 48

[167] Y. Wang, A. Suna, W. Mahler, and R. Kasowski. **Electron-electron and electron-hole interactions in small semiconductor crystallites: The size dependence of the lowest excited electronic state**. *J. Chem. Phys*, (87):7315, 1987. 48

[168] A. Lipovskii, E. Kolobkova, V. Petrikov, I. Kang, A. Olkhovets, T. Krauss, M. Thomas, J. Silcox, F. Wise, Q. Shen, and S. Kycia. **Synthesis and characterization of PbSe quantum dots in phosphate glass**. *Appl. Phys. Lett.*, **71**(23), 1997. 48

[169] G. Pellegrini, G. Mattei, and P. Mazzoldi. **Finite depth square well model: Applicability and limitations**. *J. Appl. Phys.*, **97**(7):–, 2005. 48

[170] L. E. Brus. **Electron-electron and electron-hole interactions in small semiconductor crystallites: The size dependence of the lowest excited electronic state**. *J. Chem. Phys*, (80):4403, 1984. 52

[171] A. L. Efros. *Sov. Phys. Semicond.*, (16):772, 1982. 52

[172] S.-Q. Zhan, H. Wan, L. Xu, W.-Q. Huang, G.-F. Huang, J.-P. Long, and P. Peng. **Native vacancy defects in bismuth sulfide**. *Int. J. Mod. Phys. B*, **28**(23):1450150, 2014. 60

[173] F. Furche, R. Ahlrichs, C. Httig, W. Klopper, M. Sierka, and F. Weigend. **Turbomole**. *Wiley Interdisciplinary Reviews: Computational Molecular Science*, **4**(2):91–100, 2014. 61

[174] Axel D. Becke. **Density-functional thermochemistry. III. The role of exact exchange**. *J. Chem. Phys.*, **98**(7):5648–5652, 1993. 61

[175] M. E. Casida. In D. P. Chong, editor, *Recent Advances in Density Functional Theory. Vol. I*. World Sci., Singapore, 1995. 62

[176] C. Caddeo, G. Malloci, F. De Angelis, L. Colombo, and A. Mattoni. **Optoelectronic properties of (ZnO)60 isomers**. *Phys. Chem. Chem. Phys.*, **14**:14293–14298, 2012. 62

[177] G. Konstantatos, L. Levina, J. Tang, and E. H. Sargent. *Nano Lett.*, (8):4002, 2008. 62

[178] D. Zhitomirsky, M. Furukawa, J. Tang, P. Stadler, S. Hoogland, O. Voznyy, H. Liu, and E.H. Sargent. **N-Type Colloidal-Quantum-Dot Solids for Photovoltaics**. *Adv. Mater.*, **24**(46):6181–6185, 2012. 62

[179] L. Lutterotti and S. Matthiers. *H.-R. Wenk JUCr News*, (21), 1999. 63

[180] R. Delhez, T. H. de Keijser, J. I. Langford, D. Lour, E. J. Mittemeijer, and E. J. Sonneveld. *The Rietveld Method*. 63

[181] W. A. Dollase. *J. Appl. Cryst.*, page 267, 1986. 63

Declaration

I herewith declare that I have produced this paper without the prohibited assistance of third parties and without making use of aids other than those specified; notions taken over directly or indirectly from other sources have been identified as such. This paper has not previously been presented in identical or similar form to any other examination board.

The thesis work was conducted from March 2012 to March 2015 under the supervision of Prof. Giovanni Bongiovanni at Dr. Alessandro Mattoni.

CAGLIARI, March 1^{st} 2015